Boundary Layer Dynamics after Rain Fronts: High-Resolution Reconstruction and Model Validation using ground- and drone-based Measurements

Lasse Moormann[1], Friederike Fachinger[1], Frank Drewnick[1], Holger Tost[2]
[1]Multiphase Chemistry Department, Max Planck Institute for Chemistry, Mainz, 55128, Germany
[2]Institute for Atmospheric Physics, Johannes Gutenberg University, Mainz, 55128, Germany

Correspondence to: Holger Tost (tosth@uni-mainz.de)

Abstract

Understanding atmospheric processes is essential for improving weather forecasts and models, but in continental regions the effects of dynamical mixing and frontal events on the chemical composition of the planetary boundary layer (BL) remain poorly characterized.~~Understanding atmospheric processes enables enhancing weather forecasts and models. Research in polluted areas showed that severe rain fronts influence pollutant distribution and chemical processes in the planetary boundary layer, while studies at continental rural mid-latitude sites emphasized stratification's impact on pollutants, but neglected the influence of rain fronts.~~ This study connects meteorological and chemical ~~boundary layer~~BL processes during summer rain in Central and Southern rural Germany, focusing on two events: a warm front in a high-pressure system and a cold front following a convergence line.

By combining near-hourly drone-based vertical profiles of the lowest 500 m, continuous ground-based observations, and ICON forecast model data, a detailed assessment of tropospheric dynamics for both events was achieved~~. Findings reveal~~ showing that delayed nocturnal ~~boundary layer~~BL breakup and poor vertical mixing result in weakly oxidized organic aerosol and reduced secondary aerosol formation near ground. Suppressed vertical mixing in the morning delays daytime chemical processes. A temporary post-rain O_3 depletion was linked to possible reaction with surface emission~~A temporary reduction of O_3 after rain was observed, likely due to depletion from reactions with surface emissions~~, until mixing restored vertical homogeneity.

The ICON model accurately predicted the mixing layer height under stable conditions, but underestimated it during cold pool formation with rain showers and thunderstorms. The in-situ measurements indicate the occurrence of cold pools, subsequent convective activity and disturbances of the BL dynamics.~~In-situ measurements indicate that cold pool dynamics enhance subsequent convective development.~~ Analyzing these events help to reduce uncertainty of model simulations and enhance the planetary BL parameterization. These findings enhance the understanding of air mass exchange and precipitation's effects on the lower rural troposphere as well as frontal weather scenarios and atmospheric composition changes, linking local experimental and model forecast observations to larger-scale synoptic situations.

hat formatiert: Tiefgestellt

1 Introduction

Understanding the details of atmospheric processes during different weather events is crucial for improving weather prediction, climate modelling, and environmental risk assessments (Chen et al., 2008; Wei et al., 2011; Sziroczak et al., 2022). Fronts, particularly warm and cold fronts, play a fundamental role in shaping local and regional weather conditions in the mid latitudes, influencing temperature gradients, wind patterns, and precipitation, as well as the chemical composition of the atmosphere especially near the Earth's surface.

The formation of near-surface air mass layers is a critical factor in atmospheric dynamics, as these layers control energy exchange, moisture fluxes, and pollutant dispersion. The structure of these layers is influenced by surface heating, turbulence, and synoptic-scale forcing, leading to variations in stability and mixing. During the night, radiative cooling at the surface leads to stable stratification referred to as nocturnal boundary layer (NBL), reducing vertical mixing and fostering the formation of temperature inversions. This NBL dissipates due to convective forcing and forms a convective boundary layer (CBL). The evolution of the ~~NBL~~boundary layers during frontal passages is particularly complex, as stability transitions and wind shear interactions can enhance turbulence intermittency and alter mixing processes, which can have significant implications for local weather phenomena, distribution of trace species, and air quality (Stull, 1988). A thorough understanding of these dynamics is essential for improving numerical weather prediction and refining models of boundary layer processes.

While synoptic-scale models provide valuable insights into these phenomena, accurately capturing the fine-scale interactions within the atmospheric boundary layer remains a significant challenge (Steeneveld, 2014; Qian et al., 2016; Golzio et al., 2021; Sziroczak et al., 2022). Ground-based and aerial measurement approaches offer the potential to bridge this gap by providing spatial and temporal high-resolution data on key atmospheric variables (McWilliams et al., 2023; Moormann et al., 2025).

~~The formation of near-surface air mass layers is a critical factor in atmospheric dynamics, as these layers control energy exchange, moisture fluxes, and pollutant dispersion. The structure of these layers is influenced by surface heating, turbulence, and synoptic-scale forcing, leading to variations in stability and mixing. During the night, radiative cooling at the surface leads to stable stratification referred to as nocturnal boundary layer (NBL), reducing vertical mixing and fostering the formation of temperature inversions. The evolution of the NBL during frontal passages is particularly complex, as stability transitions and wind shear interactions can enhance turbulence intermittency and alter mixing processes, which can have significant implications for local weather phenomena, distribution of trace species, and air quality (Stull, 1988). A thorough understanding of these dynamics is essential for improving numerical weather prediction and refining models of boundary layer processes.~~

Measurement towers, equipped with sonic anemometers and radiometers, offer continuous, wind profiles, high-frequency turbulence, and thermodynamic data at fixed locations but are limited by their inability to capture spatial variability and typically cover a very limited vertical range (Andreae et al., 2015). Radiosondes provide detailed vertical atmospheric profiles deep into the stratosphere, yet they only offer snapshots or incur high costs when frequently launched (Helbig et al., 2021). ~~The Monin-Obukhov Similarity Theory is capable of extrapolating near-surface measurements to different heights under quasi-stationary conditions, though it struggles with rapidly changing stability regimes and complex terrains (Monin and~~

~~Obukhov, 1954; Markowski et al., 2019).~~ Meanwhile, remote sensing techniques like lidar, sodar, and radar deliver high-resolution spatial and temporal profiles of wind, turbulence, and aerosol distributions without physical contact, but they are constrained by limitations in resolving fine-scale turbulence, signal penetration issues, and reduced precision near the surface, especially under challenging atmospheric conditions (Kotthaus et al., 2023).

Recent advancements in atmospheric science have led to the integration of drone-based observations and ~~large~~large-scale numerical weather models to enhance the understanding of boundary layer dynamics. Drones provide flexible, spatially highly resolved measurements of temperature, humidity, and wind as well as trace gases and aerosol particles at multiple altitudes, offering a valuable complement to ground-based instruments (Bonne et al., 2024; Radtke et al., 2024; Moormann et al., 2025). When combined with numerical weather prediction models, these measurements can improve the representation of sub-grid scale processes and help validate model simulations (Szintai et al., 2010; Zum Berge et al., 2023). However, challenges remain, including limited flight durations, regulatory constraints, and the need for robust data assimilation techniques (Elston et al., 2015; Villa et al., 2016; Moormann et al., 2025).

Previous studies have investigated frontal events with large scale model data or use large data sets of local data at ground level or measurement towers. While model data lack the high spatial resolution in the planetary boundary layer ~~(PBL)~~(PBL, Lochbihler et al., 2021), in-situ measurements are usually limited to specific meteorological variables, while chemical markers and frontal influence on the air mass' chemical composition is neglected. Large data sets of local data cover underlying dynamics of different rain fronts, however, they often do not cover a sufficient vertical range (Bopape et al., 2021; Helbig et al., 2021; Wang et al., 2021) or focus on different ecosystems such as tropical rainforest (Machado et al., 2024a; Machado et al., 2024b) ~~(Bopape et al., 2021; Helbig et al., 2021; Wang et al., 2021; Machado et al., 2024b; Machado et al., 2024a)~~. The influence of entrainment at the PBL top on the chemical composition has been examined (Platis et al., 2016; Pohorsky et al., 2025), but, to our knowledge, detailed analyses that couple PBL dynamics with precipitating frontal passages under midlatitude continental-plain conditions are scarce.

Feldfunktion geändert

Feldfunktion geändert

This study investigates and aims to reconstruct atmospheric processes during two distinct, but common weather events – a warm front in a stable high-pressure system (Sect. 3) and a cold front in a convergence zone (Sect. 4) – by integrating ground-based measurements, drone-based observations, and synoptic local-scale model data (Sect. 2). While the measurements provide a large comprehensive data set of the local meteorology as well as gas and aerosol trace matter characteristics with high temporal resolution, the model contributes the greater regional-scale picture. A detailed analysis of various variables derived from these complementary data sources leads to a complex overview of processes, providing a more comprehensive understanding of frontal dynamics, short and longer-term impacts of rain, and the limitations of existing observational and modelling approaches.

2. Methodology

Data from two measurement campaigns (BISTUM23, August 2023 and BISTUM24, June 2024) were analyzed to understand the influence of rain events on stratification and dynamical processes in the lowermost troposphere. A warm front in a stable high-pressure system (case 1, Sect. 3) and a cold front in a convergence zone (case 2, Sect. 4) were selected as examples of two kinds of rain events, which originate from different large-scale meteorological conditions and allow the analysis of various post-rain processes depending on the front type. The analysis of each case follows the same approach using a) local measurements at a ground station for continuous measurements and on-board a drone for quasi-hourly vertical profiling and b) large-scale assessment of the meteorological conditions using ~~a~~ radiosonde and ICON model data.

2.1 Measurement sites

For the two campaigns BISTUM23 and BISTUM24, two rural sites in German low-mountain ranges were selected. BISTUM23 took place near the city of Albstadt in the Swabian Alb (48° 15’ N, 8° 59’ E) with the ground station at 886 m above mean sea level (a.s.l.). BISTUM24 was performed near the village of Spielberg in the Vogelsberg area with the ground station at 391 m a.s.l. (50° 19’ N, 9° 15’ E). Both sites were chosen because they are in rural areas, which lowers the risk of contamination from local anthropogenic sources. The ground stations were located at the top of a hill, close to the flank of the mountain range where the ~~aspiration~~ air mass inflow usually occurs (Fig. S1). Therefore, the topographical conditions favor orographic lifting of air masses, which can facilitate deep convective events (Barros and Lettenmaier, 1994; Liu and Kirshbaum, 2025).

2.2 Experimental data

Measurements were performed on the same three platforms for each campaign and are listed in Table A1. Continuous ground-based measurements on-board the Mobile Laboratory (MoLa, Drewnick et al. (2012)) include the O/C ratio of the organic fraction of the submicron aerosol particles, measured with an aerosol mass spectrometer, particle size distribution (merged data of a fast mobility particle sizer and an optical particle counter), particle number concentration (PNC), O_3 mixing ratio, and wind data as well as temperature, humidity, and pressure. The MoLa inlet was 6 m above ground level (a.g.l.). A ceilometer monitored the aerosol backscatter signal above the site up to 10 km a.g.l. Additionally, during BISTUM24, 3D wind measurements at 5 m a.g.l. provided sensible heat flux (Q_H) and turbulent kinetic energy (TKE) data at 30 min-averaging intervals, as recommended for fair weather and pre-storm weather (Markowski et al., 2019).

Drone-based measurements were performed with the Flying Laboratory research drone (FLab, Moormann et al. (2025)), which provides a wide particle and gas phase dataset including O_3, PNC, and meteorological data. This allows the estimation of these variables’ gradients in the lowest 500 m a.g.l. as well as the calculation of the bulk Richardson number Ri, the potential temperature θ and the equivalent potential temperature θ_{eq} in Eq. (1-3) calculated from the acceleration of gravity g, the flight height above ground level $h_{\mathrm{a.g.l.}}$, the virtual potential temperature ~~θv~~θ_{V}, and the horizontal wind speeds u and v at ground at the respective air level:

$$Ri = \frac{g(\theta_{v,air} - \theta_{v,ground})h_{a.g.l.}}{\theta_{v,air}\left((u_{air} - u_{ground})^2 + (v_{air} - v_{ground})^2\right)} \tag{1}$$

θ and θ_{eq} were calculated/approximated with the air temperature T in K, the ambient pressure p, the reference pressure p_0 = 1000 mbar, the dry adiabatic constant $a = R/c_p$ from the ideal gas const. R and the heat capacity c_p of dry air at a constant pressure. Evaporation was considered in θ_{eq} with the latent heat at 20° L_{v} (20°C) = 2500 kJ kg^{-1} the specific heat for dry air C_{p} = 1004 J kg^{-1} and the total water mixing ratio r_{H2O} (Stull, 1988):

$$\theta = T \times \frac{p_0}{p}^a \tag{2}$$

$$\theta_{eq} \approx \left(T + \frac{L_v}{Cp} \times r_{\mathrm{H2O}}\right) \times \frac{p_0}{p}^a \tag{3}$$

Data from radiosondes, launched from the same site (Valero et al., 2025), help to verify the model data analysis of the meteorological conditions on a larger scale and provide the convective available potential energy (*CAPE*) as an indicator of the vertical uplift forcing before and after the weather events as well as the elevated boundary layer heights (Stull, 1988).

2.3 Model and synoptic scale data

Large-scale synoptical information such as 24 h-backward trajectories, the mixing layer height (MLH) and radar information for the respective measurement site were derived as described in the following from data sources listed in Table A2. The trajectories in Fig. S2 were calculated for 24 h-backwards with the HySplit analysis tool to detect source regions outside Germany and were started from 0 m, 120 m and 500 m above ground level (Stein et al., 2015). Besides the HySplit trajectories driven by 0.25°-GFS analysis data, ICON-D2 analysis and hourly forecast data for the gaps between the analysis time events (3 hourly) were utilised to calculate corresponding ~~mixing layer heights~~MLHs, ~~and~~ backward trajectories within the German domain and to validate the coarse HySplit trajectories (Figs. S3 and S4). ICON-D2 is the operational weather forecasting model of the German Weather Service (DWD)~~ and provides detailed weather information on a horizontal grid width of approximately 2 km~~. ICON-D2 is a non-hydrostatic model, with parameterisations for shallow convection and a sophisticated boundary layer and surface exchange scheme. Even though ICON-D2 itself operates on a triangular grid, the data has been re-gridded to a regular longitude-latitude grid with a similar grid width to ICON-D2. A detailed description of the ICON model has been provided by (Zängl et al., 2015; Crueger et al., 2018) and further descriptions are available at (DWD, 2025b).
ICON-D2 uses terrain-following Gal-Chen coordinates, according to (Klemp, 2011), with 60 vertical levels in total. The lowest kilometer above ground for the Albstadt site is described with 16 vertical levels, whereas for Spielberg 15 levels cover the lowest kilometer with corresponding layer thicknesses between 30 m close to the surface and 100 m in 1 km altitude above ground. Turbulence and surface exchange processes are parameterised with a second-order scheme following Raschendorfer (2001).

hat formatiert: Tiefgestellt

hat formatiert: Schriftfarbe: Automatisch

hat formatiert: Schriftfarbe: Automatisch

hat formatiert: Schriftfarbe: Automatisch

hat formatiert: Schriftfarbe: Automatisch

hat formatiert: Schriftfarbe: Automatisch

hat formatiert: Schriftfarbe: Automatisch

hat formatiert: Schriftfarbe: Automatisch

hat formatiert: Schriftfarbe: Automatisch

hat formatiert: Schriftfarbe: Automatisch

hat formatiert: Schriftfarbe: Automatisch

hat formatiert: Schriftfarbe: Automatisch

hat formatiert: Schriftfarbe: Automatisch

hat formatiert: Schriftfarbe: Automatisch

hat formatiert: Schriftfarbe: Automatisch

hat formatiert: Schriftfarbe: Automatisch

hat formatiert: Schriftfarbe: Automatisch

hat formatiert: Schriftfarbe: Automatisch

hat formatiert: Schriftfarbe: Automatisch

hat formatiert: Schriftfarbe: Automatisch

hat formatiert: Schriftfarbe: Automatisch

hat formatiert: Schriftfarbe: Automatisch

hat formatiert: Schriftfarbe: Automatisch

hat formatiert: Schriftfarbe: Automatisch

hat formatiert: Schriftfarbe: Automatisch

hat formatiert: Schriftfarbe: Automatisch

hat formatiert: Schriftfarbe: Automatisch

hat formatiert: Schriftfarbe: Automatisch

hat formatiert: Schriftfarbe: Automatisch

hat formatiert: Schriftfarbe: Automatisch

To obtain a higher temporal resolution than the 3 hourly analysis data, forecasts for the respective two hours in between the analysis time spots have been merged with the analysis data set, i.e., forecasts with up to 2 h lead time. The forecast data was obtained from the PAMORE data archive (DWD, 2025a) for the duration of the campaign.

The backward trajectories in Figs. S3 and S4 have been calculated using a tailored trajectory program, which regrids the model data to a regular latitude-longitude-altitude grid, including the respective grid elevation of the orography. The trajectories themselves were calculated based on a 1 min-timestep, and were finalised when the trajectory left the domain of ICON-D2 or after 24 hours.

The MLH is selected as the lowest altitude where all the following criteria in the ICON-D2 data are fulfilled: Brunt–Väisälä frequency > 5×10^{-5} s^{-1}, vertical gradient of potential virtual temperature > 0.3 K km^{-1}, and vertical gradient of absolute humidity must be curved (Wang and Wang, 2014) with threshold values empirically determined by the analysis of the simulated profiles in conjunction with the local observations and Hyun et al. (2005).~~(Hyun et al., 2005; Wang and Wang, 2014).~~

Additional synoptic scale information, displayed in Figs. S5 and S6 (surface pressure, geopotential in 500 hPa), for the selected events has been obtained from ERA5 reanalysis data (Hersbach et al., 2020) as well as from radar data (WN data set) from the radar network of the DWD (e.g., Kreklow et al. (2019)). The radar and trajectory data were obtained from the DWD data server (DWD, 2025c) during the campaigns. The respective satellite images are obtained from EUMETSAT from the MSG SEVIRI instrument (Schmetz et al., 2002)~~ instrument~~. Frontal lines in Figs. S5 and S6 were manually added to highlight areas of strong baroclinicity following the DWD analysis charts and maps of the equivalent potential temperature from ICON simulation data.~~highlight strong pressure gradients.~~

3 Case study I: ~~Delayed breakup of NBL~~Suppressed extension of a fresh CBL during warm front rain in high-pressure system

Our first case study took place at 20 June 2024 at the Spielberg site. It ~~focuses~~ combines synoptic conditions (Sect. 3.1), local turbulence measurements (Sect. 3.2 and drone-based measurements for a~~on the basic~~ characterization of different air masses (Sect. 3.3) ~~and investigates~~to reveal how strong stratification can suppress turbulence and further ~~delay the breakup of the NBL~~extension of the CBL until the afternoon. In Fig. 1, a schematic reconstruction provides an overview of underlying processes and stratification dynamics. Individual aspects are explained in the following subsections. ~~This situation took place at 20 June 2024 at the Spielberg site.~~Note, the following height ranges describe the height above ground level and time is given in local time (LT = UTC + 2 h), unless otherwise noted.

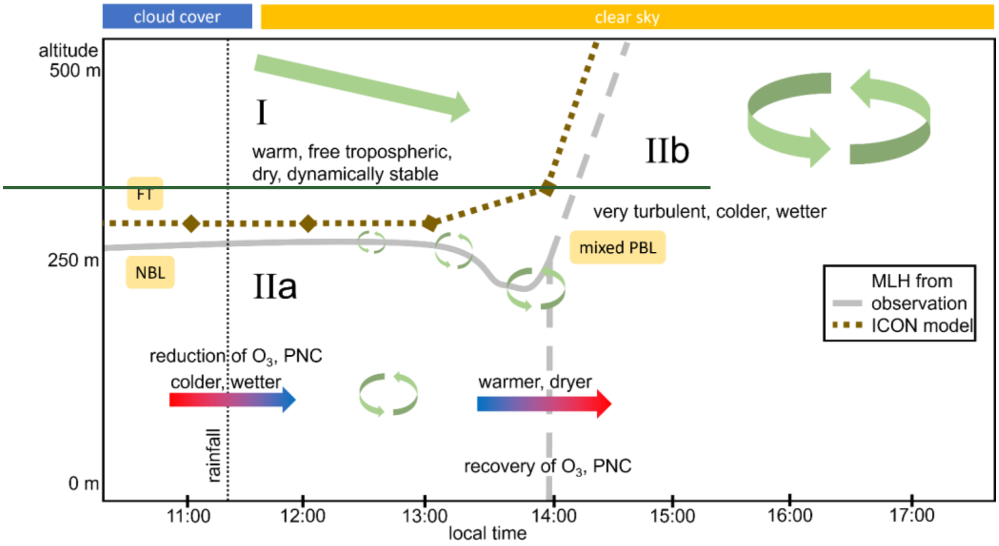
cloud cover
clear sky
altitude
500 m
250 m
0 m
I
warm, free tropospheric,
dry, dynamically stable
IIb
FT
very turbulent, colder, wetter
mixed PBL
NBL
IIa
MLH from
observation
ICON model
reduction of O_3, PNC
colder, wetter
warmer, dryer
rainfall
recovery of O_3, PNC
11:00
12:00
13:00
14:00
15:00
16:00
17:00
local time

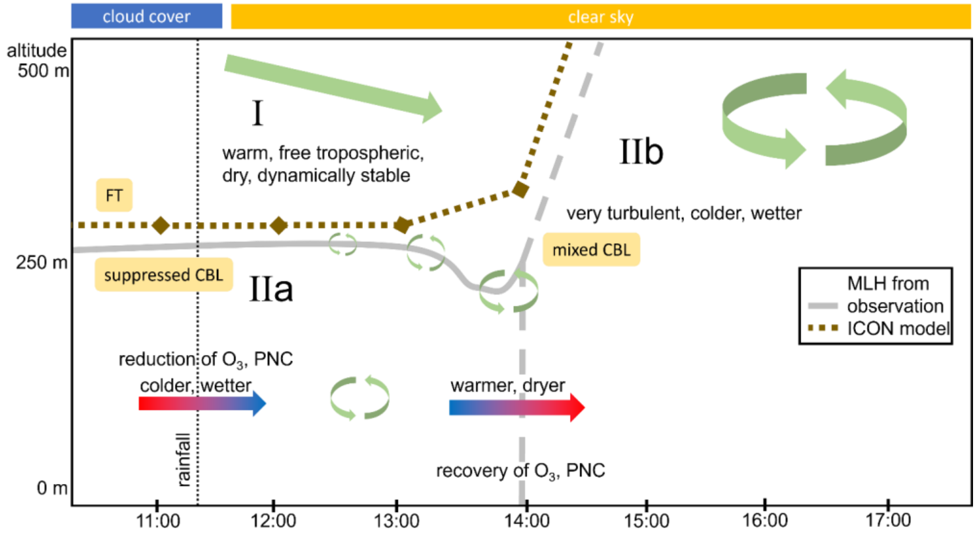
cloud cover
clear sky
altitude
500 m
250 m
0 m
I
warm, free tropospheric,
dry, dynamically stable
IIb
FT
very turbulent, colder, wetter
mixed CBL
suppressed CBL
IIa
MLH from
observation
ICON model
reduction of O_3, PNC
colder, wetter
warmer, dryer
rainfall
recovery of O_3, PNC
11:00
12:00
13:00
14:00
15:00
16:00
17:00

Figure 1: A reconstruction of different characteristics and dynamics of the air masses (I, IIa and IIb, separated by grey lines) observed before and after the rainfall event. The estimated MLH from the ICON model is presented in olive with markers indicating hourly time stamps and lines between the data points to guide the eyes. Greenish arrows represent dynamic processes, multi-colored arrows thermal processes.

3.1 Synoptic situation and local meteorology

The synoptic map in Fig. S5 shows that the measurement site was centrally located in a large high-pressure system that covered substantial parts of ~~western~~ Western and ~~c~~Central Europe with an indicated warm front crossing the measurement site. Two rain events with different intensities can be attributed to the warm front: first rain: ~20 min duration, 0.5 mm accumulated rainfall starting at 11:00; second rain: ~10 min duration, 0.1 mm precipitation starting at 15:20. FLab measured three vertical profiles before and five after the major rain event (Fig. 2a), allowing investigation of hour-scale influences of the rain event on the atmosphere in the lowermost 500 m a.g.l. The MLH reflects stratification in 300 m a.g.l. in the morning, so that FLab measures inside and above the mixing layer before and directly after the first rain event. After the second rain event, no profiling flights were possible due to temporary airspace restrictions. ~~Note, the following height ranges describe the height above ground level and time is given in local time (LT = UTC + 2 h), unless otherwise noted. The turbulence kinetic energy (*TKE*, red) increases in the morning, without being reduced prior to and during the first rain event, in contrast to the time series of irradiance (orange) and sensible heat flux (Q_H, pink, all 30 min averages). The strong correlation between irradiance and Q_H during the rain period indicates that there is no energy conservation at the ground. The hourly mixing layer height (ICON model MLH, gray) reflects stratification in 300 m a.g.l. in the morning, so FLab (drone flight altitude, black, 1 s data) measures inside and above the NBL before and directly after the main rain event (blue, 1s data).~~

At 500 hPa a stable ridge was located above ~~central~~ Central Europe, leading to large-scale subsidence. Radio soundings before and after the rain event show no change in tropopause height or *CAPE* (Fig. S7), suggesting no significant change due to the front. The high-pressure system appears to be stable, and the backward trajectories show no uplift as would be expected for warm fronts, i.e., the uplift at the warm front is compensated or suppressed by the large-scale subsidence. However, from the ceilometer data a cloud uplift from 3 km to 5 km (or a trailing higher midlevel cloud) can be deduced immediately after the first rain (Fig. 2b). A strong upper free tropospheric layer (air mass I) that suppresses a trajectory uplift is shown by the local scale observation of an immediate but short-lived dynamical stabilization above the lowermost layer and its hardly changed conditions below. Despite the missing updraft transport, the rain events can indeed be described as a warm front (see Sect. 3.2 and 3.3.1). ~~The immediate but short-lived dynamical stabilization above the residual layer (RL) after the rain event and the hardly changed conditions below the RL lead to the assumption that the trajectories may not show any uplift due to a strong RL and that the rain event can indeed be described as a warm front (see Sections 3.2 and 3.3.1).~~ A follow-up rain event like the one at 15:20 is typical for warm fronts.

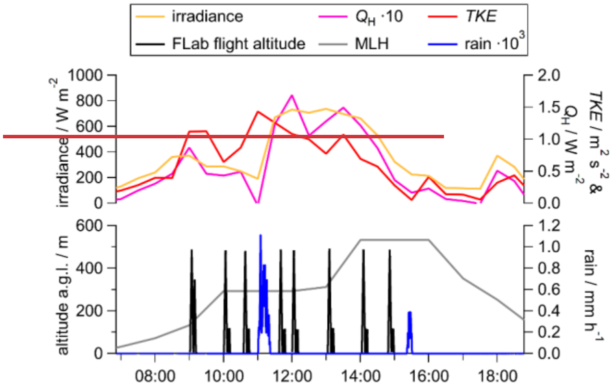

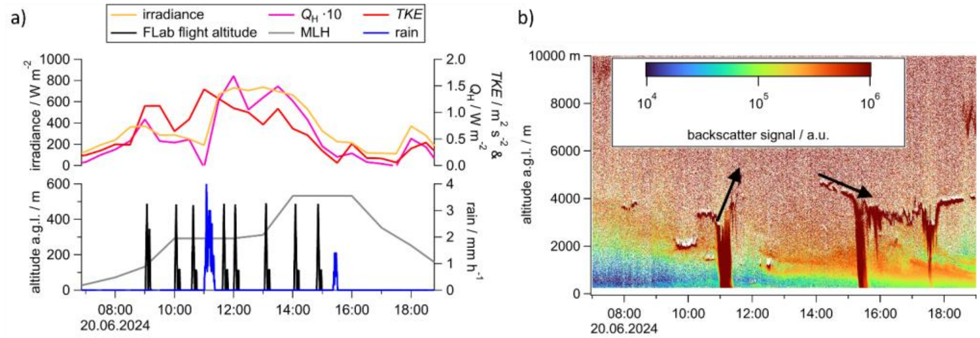

Figure 2: a) Temporal development of the ground-based measured irradiance (orange), the turbulent kinetic energy (*TKE*, red), the sensible heat flux (pink, all 30 min averages, multiplied by a factor of 10 for better visibility) and precipitation (blue) throughout the day. The hourly mixing layer height (ICON model MLH, gray) increase during the daytime, so that the FLab (flight track, black, 1 s data) was measuring below and aloft the MLH depending on the daytime. b) The ceilometer in MoLa monitors an uplift of clouds (dark red) from 3 km to 5 km immediately after the rainfall at 11:00 and a later decrease of layers before the second rainfall (red color reaching ground level indicates precipitation). Data of the lowermost 200 m were removed due to high uncertainties.

~~The turbulence kinetic energy (*TKE*, red) increases in the morning, without being reduced prior to and during the first rain event, in contrast to the time series of irradiance (orange) and sensible heat flux (Q_H, pink, all 30 min averages). The strong correlation between irradiance and Q_H during the rain period indicates that there is no energy conservation at the ground. The hourly mixing layer height (ICON model MLH, gray) reflects stratification in 300 m a.g.l. in the morning, so FLab (drone flight altitude, black, 1 s data) measures inside and above the NBL before and directly after the main rain event (blue, 1s data).~~

3.2 Driving forces of air mass mixing

hat formatiert: Schriftart:

Formatiert: Beschriftung

Stratification, such as the NBL that forms near the ground during the night, usually dissipates by midday due to convective forcing. The necessary energy for the buoyancy is provided by~~I~~ irradiance ~~is~~as the driving heat source~~ that provides the necessary energy for the buoyancy of the near ground-level NBL~~. Typically, irradiance heats the ground, which conserves energy during cloud cover or darkness, and creates turbulences in the air~~, which~~ that releases energy by dissipating eddies (Stull, 1988).

In Fig. 2a, the *TKE* increases in the morning, without being reduced prior to and during the first rain event, in contrast to the irradiance and sensible heat flux (Q_H). The strong correlation between irradiance and sensible heat flux throughout the day (Pearson correlation coefficient $r = 0.87$) ~~indicates~~ suggests that sensible heat flux is generated mainly by direct irradiance and is probably not driven by stored energy from the ground~~ (Fig. 1)~~. During the 11:00 rain event, irradiance and hence the sensible heat flux reach a minimum, while *TKE* is available independently – most likely due to advected air masses or turbulence generated by the precipitation and its evaporation itself. ~~.~~ The existing *TKE* and the small amount of sensible heat flux are not sufficient to elevate the ~~NBL~~ lowermost layer prior to rainfall. During the first two hours after rainfall, the thermal energy in the ~~NBL~~ young CBL must still accumulate before mixing ~~of the low-level residual layer~~ with the free tropospheric air can occur between 13:00 and 14:00, as the model predicts. To provide evidence for this suggested development and a more holistic understanding, the air masses in the lowest 500 m need to be characterized with in-situ data.

3.3 Characterization of different air masses

The air masses are characterized in reference to the 11:00 rain event primarily with FLab measurement data, which provide information on air mass stability and history. To reduce statistical and measurement uncertainty, the presented FLab-related data have been binned in 100 m increments for the height ranges from 0 to 500 m (~~see~~ Figs. 3 and 4). Note that strong gradients which are often measured within a few tens of meters above the ground are averaged out in the 0 to 100 m bins. To account for concentration changes over time, the O_3 and PNC data measured on-board FLab were corrected for temporal trends using the analogous continuous ground-based data measured by MoLa. The identification of different air masses (I, IIa, and IIb) and the underlying processes discussed in the following subsections lead to a schematic description of the lowermost troposphere after rainfall which is presented in Fig. 1.

3.3.1 Air mass stability

Stability indicators for vertical stratification like the bulk Richardson number *Ri* and the gradient of the equivalent potential temperature $d\theta_{eq}/dz$ are derived from FLab measurements. Air masses are considered statically unstable for negative *Ri*, dynamically unstable for positive $Ri < 0.25$, and dynamically stable, i.e., laminar, for $Ri > 0.25$, whereas a negative $d\theta_{eq}/dz$ implies instability and positive $d\theta_{eq}/dz$ stable conditions (Stull, 1988). Together with t~~T~~he *TKE* data, derived from the ground-based wind measurements (Fig. 2a)~~, show~~ consistent turbulent conditions in the lowermost 200 m in agreement with $Ri = -0.5 \pm 0.1$ and $d\theta_{eq}/dz < 0$ for all flights after the rain event (Fig. 3) are found~~)~~. A sharp increase of the *Ri*, but still negative *Ri* and $d\theta_{eq}/dz$ at 250 m altitude indicates the boundary between the two stratified statical unstable layers before the rain (Fig. 3b).

However, above 300 m, 15 min after the rain, air masses are suddenly stabilized, indicated by dθ_{eq}/dz = 38.5 K km^{-1} and contain a dynamically stable flow (Fig. 3a). The positive dθ_{eq}/dz persists at least until completion of the flight 100 minutes after the rain event and then becomes progressively negative, simultaneously with the *Ri*; i.e., dθ_{eq}/dz and *Ri* drift into a more turbulent regime in the lowermost 500 m (Fig. 3).

The upper layer can be classified as downward mixed ~~downdrafted~~ free tropospheric air (air mass I in Fig. 1), while the lower layer is probably a CBL that is formed from a dissipating~~remnant of the~~ NBL which is still present after the rain (air mass IIa in Fig. 1). The final breakup of the RL between the 3rd and ~~fourth~~ 4th flight after the rain (between 100 min and 160 min after rainfall) is induced by increasing turbulence-driven instability above 300 m as indicated by a consistent negative dθ_{eq}/dz and a decreasing *Ri*. Probably, increased convective forcing turns air mass IIa into air mass IIb (Fig. 1). Here, the continuous increase in instability with height shows that stratification is reduced such that turbulence may increase due to larger eddies at higher altitudes.

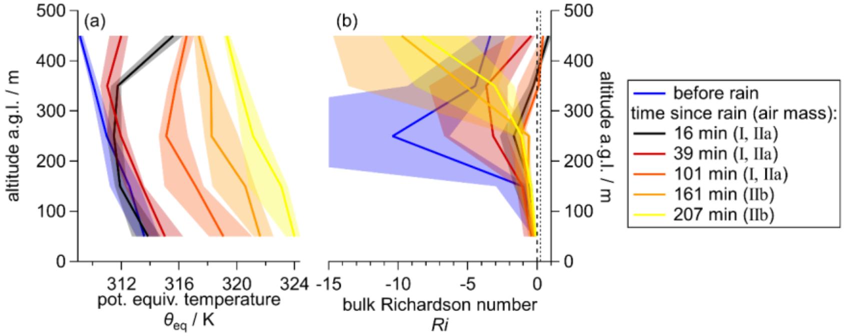

Figure ~~2~~3: The gradient of the equivalent potential temperature dθ_{eq}/dz (a) indicates unstable conditions throughout the day below 300 m, while the air mass above 300 m is stabilized after the rain at 11:00. The bulk Richardson number *Ri* (right) is consistent with a successive destabilization after the rain and indicates a stratification between 200 m and 300 m before the rain. The solid traces show the median and the shaded area is the interquartile range of the binned data. Dashed lines indicate *Ri* = 0 and *Ri* = 0.25.

3.3.2 Air mass composition and history

The air mass history like~~, e.g.,~~ travelled areas in the recent past can be determined by 24 h-backward trajectories for different altitudes. Figure ~~S7~~ S3 shows that the trajectories reaching the measurement site in the lowermost 100 m a.g.l. never travelled higher than 1000 m a.s.l. during the last six hours before rainfall, while trajectories arriving above 100 m a.g.l. at the measurement site show a strong downdraft of free tropospheric air close to the ground. According to Fig. ~~4~~1, the new air ~~mass~~ mass ~~(I)~~ above 300 m is dynamically stable and differs strongly from the statically unstable air mass below 300 m before mixing (IIa and IIb in Fig. ~~4~~1). In comparison to the in-situ measurements and the model MLH, backward trajectory tracks provide useful insight into air mass movement but lack accuracy at the vertical 100 m scale.

As shown in Fig. ~~3~~4, at altitudes above 300 m, O_3 levels are increased by up to 30%, compared to those before the rainfall, and PNC decreased by up to 70% after rain for at least 100 min. ~~Contrary~~Conversely, concentrations in the lowest 300 m remain within a range of 10% for O_3 and 20% for PNC. High O_3 levels and low PNC can be attributed to a freshly ingested, clean air mass with a high-altitude origin (Neuman et al., 2012; Tsamalis et al., 2014), confirming the free tropospheric history of air mass ~~(I)~~ before convective mixing. The influence of the rain on O_3 and PNC in the near-ground layer will be discussed in Sect. 4.3 in detail. ~~After~~ Later than 100 min after the rain event no systematic gradient is observable for O_3 and PNC anymore. Consistent with the findings in Sect. 3.3.1, the stratification, observed directly after the rain event, has disappeared 2 h ~~after~~ past the rain, and no significant differences of O_3 and PNC from the 100 m measurement increments can be observed in the lowermost 500 m, confirming a well-mixed layer. In addition to the photochemical production of O_3, mixing with free tropospheric air also causes a rapid increase of O_3 at ground level (Neuman et al., 2012), potentially causing photochemical aging of the aerosol (Lambe et al., 2011), as suggested by the strong correlation (r = 0.94) that we found for the time series of O_3 levels and the O/C ratio of organic particulate aerosol measured with the ground-based MoLa (Fig. S8). This strong correlation of O_3 with aerosol aging and the observed stratification pattern show that a delayed and suppressed extension of a young CBL can also lead to a delay in the onset of daytime chemistry. An ~~Aspiration~~ inflow of already-aged aerosols as a reason for enhanced O/C ratios is unlikely due to the stability of the PM_1 concentration measured ~~in the afternoon~~at ground. ~~This strong correlation shows that a delayed breakup of the NBL can also lead to a delay in the onset of diurnal chemistry.~~

hat formatiert: Tiefgestellt

Taken these results in combination with the results shown in Fig. ~~2~~3, the freshly ingested air mass can be attributed to the laminar and dynamically stable free tropospheric air mass I; initially, the lower-level statically unstable air mass IIa below 300 m does not show indication of mixing with~~of~~ air mass I~~ with IIa~~. From 100 minutes after the rain, almost no gradients of O_3 and PNC are observed, indicating that the layering has dissipated and air masses I and IIa have mixed to form air mass IIb across the entire 500 m range (compare Fig. ~~4~~1).

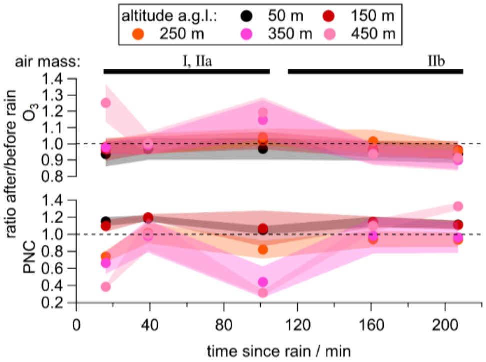

Figure ~~3~~4: The ratios of the O_3 mixing ratio (top) and the particle number concentrations PNC (bottom) after to before the rainfall (at 11:00) were calculated for different altitude increments (color-scale) for five vertical profiles measured at different times after the rain. Error bars represent the combined standard error of flights before and after the rain. Attributed air masses that are identified within a flight are indicated at the top of the graph.

3.3.3 Delayed ~~N~~CBL extension~~breakup~~

Boundary layer lifting can be limited or suppressed by overlying inversion layers and insufficient convective forcing. In addition to the low convective forcing due to low irradiance caused by the cloud cover, stratification is supported by the subsidence of air mass I, which is drier and warmer than the underlying ~~NBL~~lowermost layer. Strong wind shear drives the turbulent mixing dynamically until the temperature has increased, i.e., the energy has accumulated within the ~~NBL~~ CBL and convection-driven turbulence mixes air mass I with air mass IIa 100 min after the rain. Dissipation of the boundary between the dynamically different air masses I and IIa forms the mixed air mass IIb, as shown in Fig. ~~4~~1. Comparison of the observed stratification height from the in-situ data and the MLH derived from ICON data agrees within the model height resolution ~~(±~~ (± 70 m in 300 m, Fig. 1 ~~4~~). This demonstrates that the ICON model can forecast the MLH with high accuracy at least under relatively stable large-scale conditions.

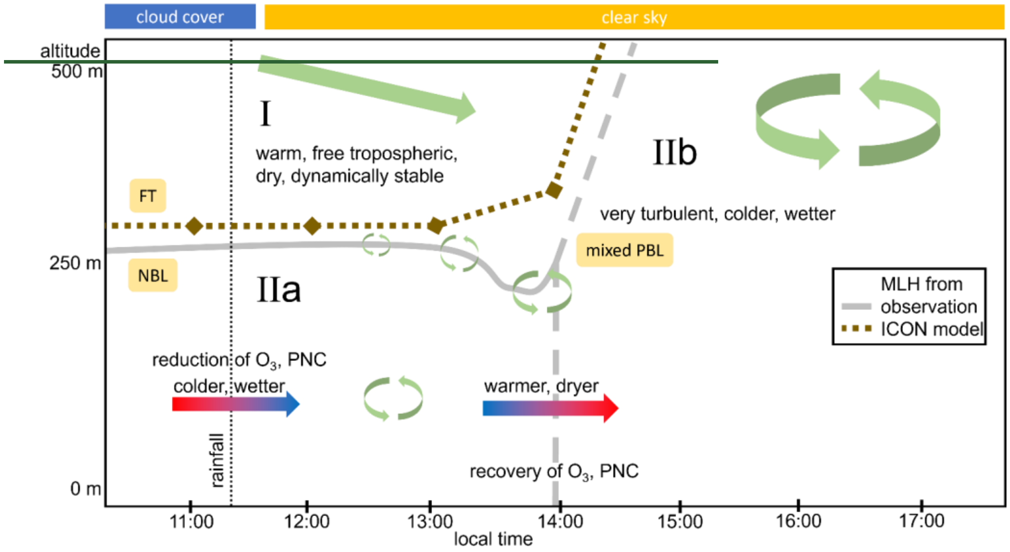

~~**Figure 4: A reconstruction of different characteristics and dynamics of the air masses (I, IIa and IIb, separated by grey lines) observed before and after the rainfall event. The estimated MLH from the ICON model is presented in olive with markers indicating hourly time stamps and lines between the data points to guide the eyes. Greenish arrows represent dynamic processes, multi-colored arrows thermal processes.**~~

4 Case Study II: Impact of a cold front and a convergence line on the lowermost troposphere

The influence of ~~To investigate how~~ thunderstorms ~~affect~~ on the pollutant distribution and air mass dynamics in the lower troposphere was investigated by vertical profiling. T~~, t~~hroughout a day when a thunderstorm occurred at the measurement site eleven FLab-based ~~vertical profiling~~ measurements were conducted hourly, as long as weather conditions allowed for safe operation. Ground-based measurements allow observation during the heavy-rain phase underneath the convergence line. Like for Sect. 3, ~~A~~an ~~summary~~overview of the temporal exchange of air masses and the accompanying processes is shown in Fig. ~~6~~5, while the underlying processes that lead to the schematic are explained in the following sections.~~.~~

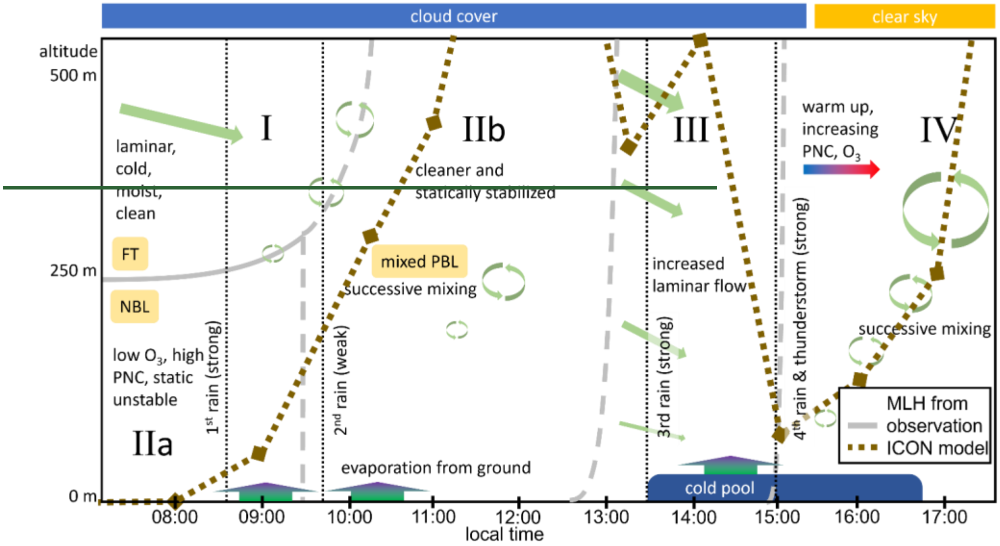
cloud cover
clear sky
altitude
500 m
250 m
0 m
laminar,
cold,
moist,
clean
FT
NBL
low O_3, high
PNC, static
unstable
IIa
I
1st rain (strong)
2nd rain (weak)
IIb
cleaner and
statically stabilized
mixed PBL
successive mixing
evaporation from ground
3rd rain (strong)
III
increased
laminar flow
cold pool
4th rain & thunderstorm (strong)
warm up,
increasing
PNC, O_3
IV
successive mixing
MLH from
observation
ICON model
08:00
09:00
10:00
11:00
12:00
13:00
14:00
15:00
16:00
17:00
local time

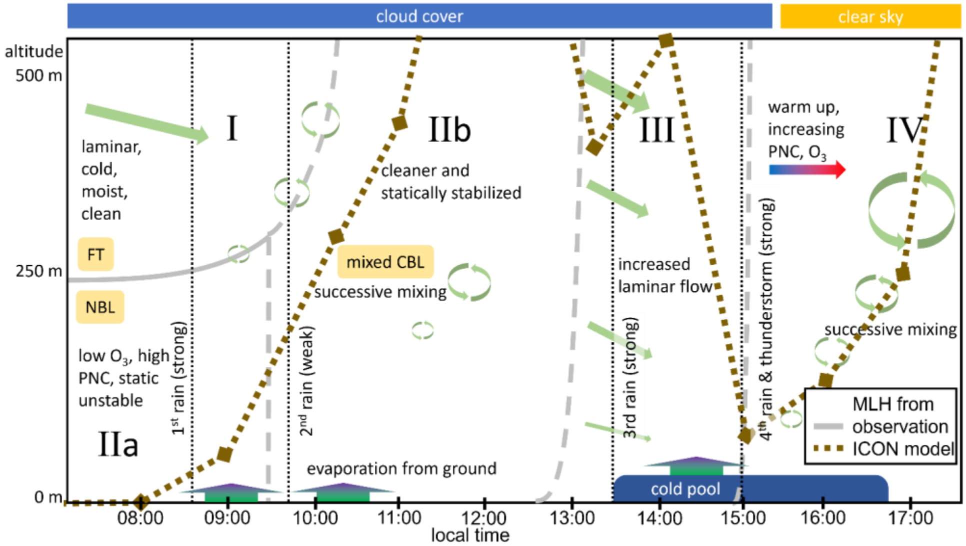
cloud cover
clear sky
altitude
500 m
250 m
0 m
laminar,
cold,
moist,
clean
FT
NBL
low O_3, high
PNC, static
unstable
IIa
I
1st rain (strong)
2nd rain (weak)
IIb
cleaner and
statically stabilized
mixed CBL
successive mixing
evaporation from ground
3rd rain (strong)
III
increased
laminar flow
cold pool
4th rain & thunderstorm (strong)
warm up,
increasing
PNC, O_3
IV
successive mixing
MLH from
observation
ICON model
08:00
09:00
10:00
11:00
12:00
13:00
14:00
15:00
16:00
17:00
local time

Figure 5~~6~~: A reconstruction of different characteristics and dynamics of the air masses (I, IIa, IIb, III, and IV, separated by grey lines; solid line illustrates stratification, dashed lines transition periods) on 12 August 2023. The estimated MLH from the ICON model (1-h resolution) is presented in olive with dashed lines between the data points to guide the eye. Greenish arrows display dynamic processes, multi-colored arrows thermal processes.

4.1 Synoptic situation and local meteorology

During ~~the~~ 12 August 2023, four precipitation events were observed at ground level at the Albstadt site, while the ceilometer recorded seven, including three that did not reach the ground due to evaporation of rain droplets at higher altitudes (Figs. ~~S9~~6a and b)~~, S10 and Fig. 5)~~. Even after the last rain event with a strong thunderstorm at 15:00, clouds were still present and the irradiance did not reach the levels of cloudless days, although the conditions became mild and the temperature rose by up to 10 °C.

For this day, synoptic maps show a convergence line and a cold front crossing the site from 14:40 to 15:20 (Figs. ~~S3 and~~ S~~10~~6). A severe thunderstorm may have been caused by the combination of substantial lability and *CAPE* in addition to orographic lifting of warm air in conjunction with the convergent flow between 14:30 ~~to~~ and 15:00. Radiosondes launched from the site recorded *CAPE* of 1400 J kg^{-1} at 14:00, while it decreased to less than 10% of this value, i.e., 130 J kg^{-1}, during mild, sunny conditions after the thunderstorm (radiosonde at 16:40, Fig. ~~S11~~S9)~~ during mild, sunny conditions~~. 24 h-backward trajectories ~~(calculated with Hysplit,~~ (calculated with HySplit, Stein et al., 2015)~~)~~ indicate ~~aspiration~~ inflow of air masses, amongst other across the mountain ranges of the Black Forest and the Swabian Alb, during the 100 km long track before they reached the measurement site (Figs. S2~~4~~ and S~~12~~4).

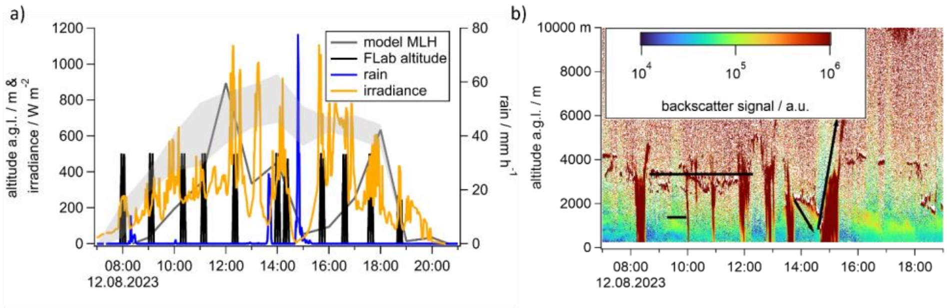

Figure 6: a) Time series of irradiance (orange), precipitation (blue, both 1 min averages), and the modelled MLH (grey, hourly averages) on 12 August 2023. The flight altitude of FLab is displayed in black. The shaded area represents the typical diurnal cycle of the modelled MLH at the BISTUM23 measurement site for cloudless days. b) The ceilometer in MoLa monitors a stable cloud layer between 3 to 4 km altitude a.g.l. and frequent rain events throughout the day (indicated by dark-red color). Before the thunderstorm at 14:30, a decreased cloud layer down to 1 km a.g.l. is observed, followed by a quick uplift to 7 km. Data of the lowermost 200 m were removed due to high uncertainties.

4.2 Reconstruction of air mass exchange by cold fronts and a convergence line

In this subsection, similar to the approach for Fig. ~~4~~ 1 (Sect. 3) we develop an overview schematic that describes the details of the boundary layer processes around the investigated event (Fig. ~~6~~5). The schematic contains air masses characterized by dynamical and chemical properties, which are tagged with roman letters (I, IIa, IIb, III, and IV) and should not be confused with the air masses mentioned in the previous Sect. 3.

The meteorological situation of the boundary layer on 12 August 2023, can be separated into a dynamically unstable pre-thunderstorm period and a stable post-thunderstorm period. In contrast to the situation described in Sect. 3, no ground-based flux measurement data are available. A consistent $Ri = 0$ at the 50 m mark during all times when the Flab was operating indicates unstable conditions, i.e., small-scale turbulence at the ground, which are not significantly influenced by processes above 100 meters (Fig. 7~~5~~a). Before the first rain event at 08:30, a layer boundary at the 250 m mark was identified by sign changes of the weak gradients for Ri, potential temperature, absolute humidity, O_3, and PNC (Fig. S1~~3~~0 or orange dots in Fig. ~~5~~7). While positive gradients of potential temperature and Ri indicate increasing dynamic stability with altitude, the upper air mass above 200 m is classified as laminar with $Ri = 0.6$ with enhanced moisture and O_3 levels (O_3 increased by 6 ppbv), and reduced particulate pollution (PNC decreased by > 1000 particles cm^{-3}). Here, free tropospheric air (I in Fig. ~~6~~5) overlays a weak NBL remnant ~~(IIa in Fig. 6)~~ above 200 m (IIa in Fig. 5), similar to the case in Sect. 3.

After the first rainfall event (0.5 mm in 15 min), the NBL remnant remains present, reaching heights of up to 200 m as predicted by ICON. However, the air mass I above the NBL remnant becomes more stable (increasing Ri and $d\theta_{eq}/dz$) after the rainfall event. Before 10:00, it rises to a height of 1100 m, where the ceilometer detects the upper boundary of an aerosol layer (~~see~~ Fig~~.~~. ~~S10~~6b).

After a light second rainfall of 0.1 mm at 10:00, no RL and uniform gradients are observed over the whole 500 m-altitude range for all FLab-measured variables until 13:00. In air mass IIb mixing has eliminated the gradients. Since the first two rain events at 08:30 and 10:00, potential temperature near ground has increased by only 2-3 K, suggesting that diurnal heating primarily contributes to latent heat rather than driving vertical mixing (Fig. ~~5c~~7c). This observation is in agreement with very slow evaporation from moist soil that might explain the unusually stable equivalent potential temperature at the 50 m mark between 10:00 and 13:00 (Fig. ~~5b~~7b), while the difference to the potential temperature decreases (Fig. ~~5c~~7c). A similar pattern is observed for the last rain event, although here evaporation is accelerated by strong irradiance and turbulence-driven mixing. At 13:30, a cold front delivered 2.4 mm of rain in 10 minutes leading to a 2.2 °C decrease in air temperature and 2.1 g kg^{-1} increase in humidity at ground, while equivalent potential temperature remains constant at ground ~~,~~ as measured with MoLa (Fig. ~~S14~~8). However, at 50 m altitude and above no change in temperature, humidity, and ~~the~~ $d\theta_{eq}/dz$~~vertical gradient of equivalent potential temperature~~ is observed. The slow evaporation of moisture from previous rainfall forms a localized moist patch, which, on a regional scale, might develop into a cold pool. Cold pools can create a positive feedback loop: ~~T~~they generate broader clouds that are less affected by entrainment, leading to increased precipitation, larger moist patches, and further expansion of cold pools – ultimately fostering larger clouds with enhanced convective mass fluxes (Schlemmer and

Hohenegger, 2014). ~~Tompkins (2001) shows that along an already recovered cold pool, the increased equivalent potential temperature (here increased by 6 K at ground and by 2.1 K at the 50 m altitude bin, Figs. 5b and S14) and water vapor trigger new convective cells, like the upcoming rain front in this case study.~~ Simulations of cold-pool dynamics indicate that, under continental conditions in the mid latitude, strong latent heat flux can increase convective mass flux (Lochbihler et al., 2021). In our case, following the rain events at 13:30 and 14:45, we observe a cold pool from ground~~-~~ and FLab measurements, identified based on four indicators: (i) stratification between the lowermost 100 m (cold pool) and aloft is visible for the dynamical markers $d\theta/dz$ and *Ri* (Fig. ~~5a~~7a, c) as well as for the O_3 mixing ratio (ii), which is ~~~10~~ (5.3 ± 3.4) pptv (~~20~~12%) lower in the lowermost layer (Fig. ~~5e~~7e, ~~). P~~presumably due to depletion in the wet cold pool); (iii)~~. T~~ the increased negative gradient and variance of the absolute humidity (Fig. ~~5d~~7d) and (iv) an increase of the equivalent potential temperature by ~6 K at ground and by 2.1 K for the whole 500 m range ~~up to 500 m~~ (Fig. ~~5b~~7b) show the evaporation and conditional enhanced latent heat flux typical for cold pools ~~and conditional enhanced latent heat flux~~ (Tompkins, 2001; Engerer et al., 2008). These highly-resolved vertical observations between 13:30 and 14:45 support the model-based hypothesis by Lochbihler et al. (2021) and Haerter and Schlemmer (2018) that strong latent heat flux and associated evaporation can promote the formation of new convective cells like the upcoming rain front for our case study. ~~(Lochbihler et al., 2021; Tompkins, 2001; Haerter and Schlemmer, 2018)~~Due to increased latent heat flux, thermal convection is suppressed initially, leading to a homogeneously laminar air mass III with *Ri* = 0.28 above 100 m, while air in the lowest 100 m is dynamically stable due to surface roughness. The downdraft of air mass III is likely enhanced by the cold pool, as penetrative downdrafts from the mid-troposphere commonly occur after rainfall exceeding 2 mm h^{-1} (Barnes and Garstang, 1982), in agreement with model results under convergence zone conditions (Schlemmer and Hohenegger, 2014).

At 14:30 the last rain event of the day with 5.4 mm precipitation in 40 min was associated with a severe thunderstorm under a convergence line as described in Sect. 4.1. Despite the reduced *CAPE* after the storm (>90% decrease), the new air mass IV remains unstable. Unlike the unstable air mass III, which might be unstable due to deep-convective vertical forcing (*CAPE*), this air mass IV is likely unstable due to small-scale turbulence indicated by a suddenly negative *Ri* above 100 m altitude and a remaining negative $d\theta_{eq}/dz$ from 15:30 on (Fig. ~~5a~~7a, b). Additionally, the convection did not take place in a frontal system, thus the existing air mass was not replaced by a colder, more stable air mass. Instead, only a part of the *CAPE* was consumed by the convective event which was initiated and substantially driven by the convergence. After the rain event, the post-convective subsidence led to cloud free conditions and thus growing instability caused by irradiance and enhanced ground temperatures (Fig. ~~S14~~8). Higher temperatures and thermally driven convection at the ground allow for drying of the moist near-ground layer, and for recovery of the lowermost troposphere from the thunderstorm as thermal mixing removes the vertical gradients of potential temperature, absolute humidity, PNC and O_3 after the last rain event (Fig. ~~5~~ 7c-f). ~~A summary of the temporal exchange of air masses and the accompanying processes is shown in Fig. 6.~~

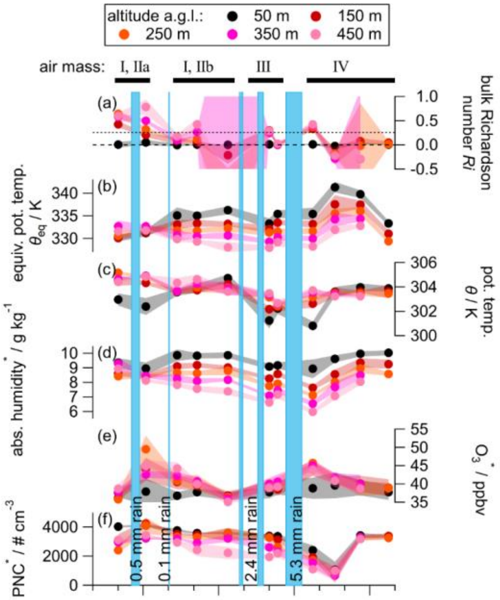

Figure ~~5~~7: Development of medians of 100 m altitude increments of the bulk Richardson number *Ri* (a), equivalent potential temperature θ_{eq} (b), potential temperature θ (c), absolute humidity (d), O_3 mixing ratio (e), and the particle number concentration (PNC, f) with time on 12 August 2023. Variables marked with * are corrected for temporal variation using the corresponding MoLa data. Error bars are derived from interquartile ranges. Dotted lines indicate *Ri* = 0 and *Ri* = 0.25. Rainfall periods are marked in blue with the amount of rain noted (precipitation at 13:00 and 14:00 were summed).

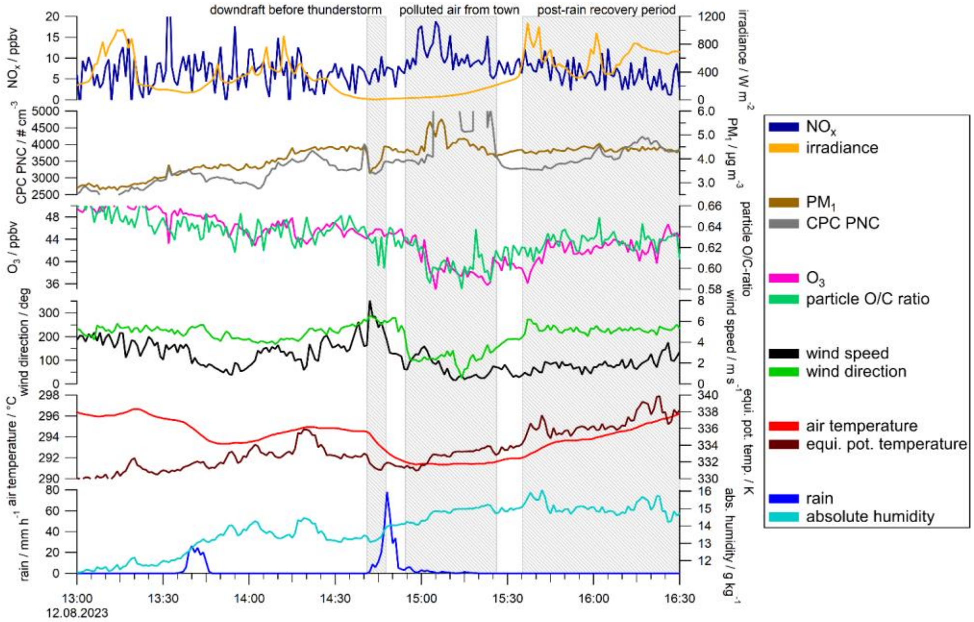

Figure 8: 1 minute-time series of PM_1 (light brown), and wind speed (dark green), measured on-board MoLa, show clean air advection before rainfall (blue). After the thunderstorm, the wind direction changes (light green) affecting measured NO_x (dark blue), particle number concentration (PNC, grey), O_3 (pink) and the O/C ratio of PM_1 organics (green). As the irradiance (yellow) increases, the absolute humidity (turquoise) also increases due to evaporation of water from ground. Descriptions of various periods are given above the shaded areas.

Formatiert: Standard

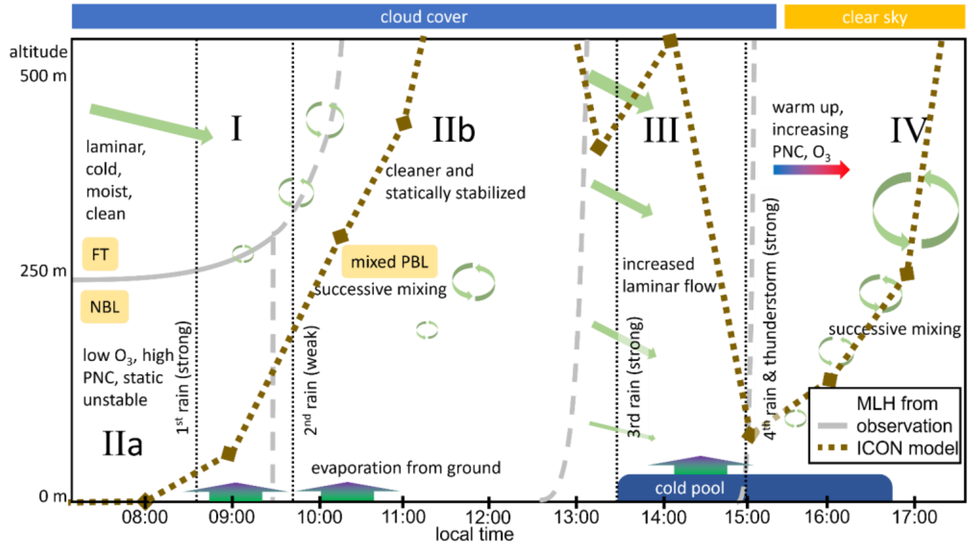

~~**Figure 6: A reconstruction of different characteristics and dynamics of the air masses (I, IIa, IIb, III, and IV, separated by grey lines; solid line illustrates stratification, dashed lines transition periods) on 12 August 2023. The estimated MLH from the ICON model (1-h resolution) is presented in olive with dashed lines between the data points to guide the eye. Greenish arrows display dynamic processes, multi-colored arrows thermal processes.**~~

4.3 Impact of rain events on pollutant distribution

During the day, four rain events with different amounts of precipitation occurred, leading to different changes in the trace matter distribution. Contrary to the morning precipitation events, when there was no lifting of air masses before they reached the measurement site, for the rainfall events at 13:30 and 14:30 the 24 h-backward trajectories show a lifting up to above 2000 m a.s.l. and a sudden downdraft~~ due to the cold pool~~, 7 h and 1 h before arrival of the air masses at the measurement site, respectively (Fig. S~~12~~4). This downdraft dynamic was also observed by the ceilometer, which measured cloud layers subsiding from 2500 m down to 700 m a.g.l prior to the thunderstorm (Fig. ~~S10~~6b). The downward motion is likely a sign of an onset of convergence leading to more low level and convective clouds and may be enhanced be the cold pool at the ground. This downdraft results in the injection of clean, O_3-rich air with low particle load into the lowermost troposphere and represents the transition to air mass III (~~Fig. 5e, f, and~~ Fig. ~~6~~5 and 7e, f).

After each rain event, O_3 mixing ratios are increased at altitudes above 200 m (due to the air mass downdraft from higher altitudes, Fig. ~~5e~~7e), but decreased near the ground by 3.0 ± 1.3 ppbv, excluding the 10:00 rainfall, as shown in Fig. ~~S15~~S11. As a consequence, O_3 gradients are enhanced by 7 ppbv km^{-1} for each rain event and subsequently disappear within a few hours due to convective mixing within the PBL. Reduced ground-level O_3 concentrations following rainfall may result from deposition or enhanced O_3 depletion, whereas outwash seems unlikely due to the poor solubility of O_3 in water, except for potential aqueous phase SO_2 oxidation (Hoyle et al., 2016). Depletion could be driven by the increased release of primary biogenic volatile organic compounds (BVOCs) from vegetation or by peroxide-scavenging after rainfall (Bela et al., 2018; Rossabi et al., 2018; Miyama et al., 2020; Machado et al., 2024a). BVOCs have been identified as an O_3 sink in natural and anthropogenic conditions (Fitzky et al., 2019; Machado et al., 2024a). However, this emission-driven O_3 removal mechanism cannot be verified due to the lack of BVOC data.

Figure ~~5f~~ 7f highlights that for the same rain events, when O_3-rich air was injected into the lowest 500 m, the CPC PNC was consistently reduced by 25% (except when the NBL was still present, because air mass I is already in the free troposphere). The PNC gradient remained unchanged during and after the regeneration period, and the PM_1 levels measured at ground remained constant immediately after rain (Fig. ~~S14~~8), indicating that washout was minimal under these conditions. This is likely due to the size of the measured aerosol particles that are in the Greenfield gap and consequentially inefficiently removed by outwash (Cherrier et al., 2017).

These observations show that rain itself does not necessarily significantly influence the distribution of pollutants such as O_3, PM_1, and PNC. However, post-rain air masses determine the composition and gradients at higher levels, while rain-induced emissions from the ground may act as a sink for reactive substances as O_3.

4.4 Influence of cold pool formation on model MLH

In Section 3 we showed that the determination of the MLH using 1-h forecast data from the ICON model is feasible with high accuracy under stable conditions during a weak warm front (Fig. ~~4~~1). The MLH estimation criteria in the model include the Brunt–Väisälä frequency, humidity, and potential virtual temperature gradients. Until this point of the study the MLH is used as a synonym for the height of the planetary boundary layer (PBLH), which is considered the most relevant measure separating the free troposphere and the ground-influenced layer with different dynamical characteristics and composition (Stull, 1988; Tignat-Perrier et al., 2020; Kotthaus et al., 2023). Note that other kinds of stratification occur regularly in the troposphere and are often not predictable, due to local topography, emissions, and heat reservoirs.

For the convergence line / cold front case analyzed in this section, the modelled MLH, shown in Figs. 5 and ~~S9~~6a ~~and also included in Fig. 6~~, increases from 0 m at 08:30 to 200 m at 10:00 and 300 m at 11:00. This observation is consistent with the NBL identified from in-situ FLab data and demonstrates additionally to Fig. ~~4~~ 1 that the MLH algorithm predicts the height of the NBL (in this case the PBLH) accurately. However, between 12:00 and 18:00, the modelled MLH drops below 500 m before returning to levels above 600 m at 18:00, where it continues following its diurnal cycle (Fig. ~~S9~~6a). The average predicted diurnal cycle of the MLH at the measurement site from Sect. 4 shows maxima of the PBL between 800 to 1000 m at 14:00 to 15:00 on clear-sky days, while being < 20 m during night (Fig. ~~S9~~6a). The difference between the modelled MLH in the cold front case, compared to the average diurnal cycle of the PBLH, may be explained by reduced irradiance (average of 100 W m^{-2} during this period).

hat formatiert: Tiefgestellt

The formation of a cold pool at ground leads to an increase of latent heat flux and consequentially to less turbulent mixing. Therefore, the cold pool acts as an energy sink and suppresses energy supply for further turbulent mixing~~suppresses energy consumption for further turbulent mixing~~. Although convection has driven the PBLH up to the free troposphere before the rain, the cold pool contributes to layering of the convective-driven RL above a shallow turbulent mixing layer. This stratification disappears as the cold pool dissolves.

hat formatiert: Englisch (Vereinigte Staaten)

These dynamic processes drastically alter the vertical gradients, and may have influenced the MLH model output, which relies solely on vertical gradients. The ICON 1-h forecast models that the MLH exceeds 500 m after 11:45 and thus differs strongly from our in-situ observations. After irradiance decreased, MLH criteria were met even below 400 m due to rapidly changing gradients caused by vertical dynamics within the convergence zone. ICON data predict a MLH of 600 m at 18:00 that can be assigned as a realistic PBLH 2.5 h after the last rain, in agreement with the mean life time of a cold pool (Tompkins, 2001). Interpolating the MLH between 12:00 and 18:00 may lead to an inaccurate estimate, because the PBLHs maximum is expected in between. In agreement, radio soundings at 14:10 and 16:40 indicate a boundary layer up to slightly above 800 hPa, i.e., 1.400 m and 1.300 m based on changing lapse rates and temperature gradients ~~(Fig. S11,~~ (Fig. S9, Seidel et al., 2010)~~)~~. The PBLH derived from the radio soundings is 100 m to 200 m higher than the estimated average MLH for the measurement site (Fig~~—~~. ~~S9~~6a), indicating that the PBLH has lifted due to convective forcing by the thunderstorm. A more robust parameterization of the MLH estimation for the PBLH for cold pool scenarios may consider two MLHs: a lower MLH separating an additional shallow cold pool-driven layer at ground from the previously well-mixed PBL and a second MLH separating the PBL from the free troposphere in the altitude range close to the PBL before rain events. Alternatively, the upper boundary of the PBL is described by a kind of "residual layer" where the cold pool leads to a different PBL structure below.

4.5 Convergence zone advection and measurement limitations

Due to unsafe flight conditions, vertical profiling during the thunderstorm was not possible; instead, ground-based MoLa data were used to analyze meteorological processes during this time (Fig. 8~~S14~~). Between 14:30 and 15:30, a strong cloud layer largely suppressed irradiance and minimized thermal convection, leading to dynamically deep convective inflow-driven air masses with surface wind speeds peaking at 8 m s^{-1}. As the rainfall starts, strong downward movement of air is implied by a descending cloud layer height, a high wind speed period, and a 40% reduction in PM_1 due to mixing in of unpolluted free tropospheric air (Figs. ~~S10~~6a and~~,~~ ~~S14~~8). Although it is known for cold pool-induced deep convective events that the horizontal wind speed is maximal before rainfall starts (Tompkins, 2001), a strong downdraft from the start of rainfall until the maximum of the precipitation rate was not described, yet, probably because observational studies describe longer-lasting rainfalls only (Young et al., 1995).

As the rain band advanced, heavy rain ceased and wind direction turned by 180°, an effect attributed to a moving convergence zone (Crook and Klemp, 2000), which changed the air track from passing a rural forest (~~western~~Western) to the town of Albstadt (~~eastern~~Eastern, Fig. S1a). This resulted in increased ~~NO_x~~ NO_X and PNC with lower aerosol oxidation levels, indicated by the reduced particulate organics O/C ratio (Fig. ~~S14~~8). After rainfall, near-surface O_3 was reduced (possibly due to depletion by enhanced anthropogenic or natural emissions as ~~NO_x~~ NO_X or BVOCs, see Sect. 4.3), though it slowly recovered as the wind direction turned back from ~~east~~ East to ~~west~~ West after 40 min. When irradiance exceeded 400 W m^{-2} at 15:35, photochemical activity led to enhanced PM$_1$ and PNC; simultaneously, temperature and absolute humidity increased as the grassland dried.

These rapid shifts in air mass history and wind dynamics behind the convergence line highlight the need of in-situ 3D turbulence observations, e.g., with wind LIDAR (Bélair et al., 2025) to fully capture local upwelling and advection processes within the PBL (Borque et al., 2020); measurements at a less polluted site (independent of wind direction) would be helpful to identify compositional changes due to the thunderstorm itself or thunderstorm-related effects like BVOC emissions from the ground.

5 Summary

By integrating hourly in-situ vertical profiles of the lowest 500 m with continuous ground-based observations, synoptic situation, and modelled PBLH, we can thoroughly analyze dynamical mixing, stratification, and thermal and chemical processes in two typical rain front scenarios in the continental mid-latitudes. Previous studies have often used remote sensing methods and focused separately on dynamical (Ryan et al., 2000; Andreae et al., 2015; Helbig et al., 2021; Luiz and Fiedler, 2024) or chemical processes in various terrains (Knote et al., 2015; Miyama et al., 2020).

Our highly-resolved in situ measurements showed an ~~significant~~ influence of the atmospheric stratification on pollutant distribution for a stable continental PBL (Platis et al., 2016; Pohorsky et al., 2025). However, the influence of rain fronts in the mid-latitudes has not been studied so far. We fill the research gap by providing a combined analysis with highly-resolved in-situ measurements in the PBL for physical and chemical processes under frontal conditions, even including a cold pool.

In the first case study, a weak warm front associated with a large-scale high-pressure system approaches the measurement site in the morning. A warm, stable, descending air mass suppresses the vertical expansion of the NBL, while shear winds suppress turbulent mixing between the free troposphere and the NBL. Precipitation further cools the surface, converting ground thermal energy into latent heat. Although irradiance gradually increases turbulent instability, it takes about 2 h after the passage of the front for the accumulated energy to lift the NBL and to form a convectively mixed boundary layer. This delayed breakup of the NBL postpones the entrainment of free tropospheric, O$_3$-rich air and the cloud cover delays the onset of daytime photochemistry into the afternoon. The ICON forecast model accurately estimates the MLH under these conditions.

In contrast, the second case study examines a synoptic cold front trailing behind a convergence line, accompanied by several rain showers and a severe summertime thunderstorm. The selected diagnostics from the ICON model underestimate~~s~~ the MLH after the passage of the convergence line during these unstable conditions. In order to understand the reason for the failure of MLH determination and improve weather prediction models, it is essential to reconstruct air mass exchange in the lowermost troposphere and to identify the tropospheric processes. During this cold front event, five air masses are identified, characterized by their dynamical, thermodynamical, and chemical properties. These observations reveal that a moist patch forms at ground after the morning rain; as it dries slowly, it promotes the development of a deep convective thunderstorm and triggers a positive feedback loop that leads to the formation of a cold pool. The recovery of vertical gradients and the dissipation of the cold pool in the lowest 500 m occurs over approximately 2.5 hours after the rain event, consistent with recovery processes observed in the tropics (Tompkins, 2001).

After precipitation events with more than 0.5 mm rain, we observed a decrease of ground-level O_3 mixing ratios, possibly due to depletion by fresh biogenic emissions; additionally, unpolluted, O_3-rich free tropospheric air is injected into the lowest 500 m. The gradients resulting from evaporation, O_3 depletion, and injection of free tropospheric air disappear within two hours after rain, driven by thermal convective mixing as temperatures and irradiance increase.

In-situ analysis and reconstructions of the lowermost troposphere reveal that air mass exchange, turbulent mixing, irradiance, and physicochemical processes each play distinct roles in defining air mass characteristics. The overview figures (Figs. ~~4~~1 and ~~6~~5) illustrate the post-frontal regeneration processes. These processes occur not only in rural rain events but also in other frontal situations under common meteorological conditions in the mid-latitudes. The physicochemical processes inside the boundary layer are assumed to be representative for similar topography (rural hilly regions and plain fields). Thus, these results have broader implications on how to consider atmospheric chemical processes and compositional change in the PBL in pollutant ~~modeling~~modelling associated with rain fronts (and cold pools) due to dynamical changes. Despite being limited to two cases with hourly resolution and no in-rain flights, the study shows that combined model- and ground-based analysis can conceptually identify complex boundary layer phenomena like pollutant sinks and local stratification. This emphasizes that high-resolution vertical data are crucial for assessing individual weather events, avoid misinterpretation, and enhance forecasting and model calculations.

Further field studies with similar vertical resolution at different locations with varying surfaces like in flatland, alpine mountains or cities could help to better characterize frontal dynamics. Reanalysis of MLHs with ICON for comparable cold pool scenarios as in Sect. 4 could allow finding a parameterization to identify and predict cold pools solely on a model basis, which is important as the occurrence of cold pools is expected to increase with climate warming in the mid-latitudes (Borque et al., 2020). This could also help to estimate the MLH more precisely under strongly unstable conditions. Recorded BVOC data from field campaigns should be reanalyzed regarding O_3 depletion after rain above grassland, where vertical O_3 measurements were available.

Acknowledgements The authors thank Thomas Böttger and Philipp Schuhmann (both Max Planck Institute for Chemistry) for support during the BISTUM23 and BISTUM24 campaign and Luis Valero (Johannes Gutenberg-University, Mainz) for providing the skew-*T* diagrams and corresponding *CAPE* values from radiosonde measurements.

Code availability The code for the FLab data acquisition and data monitoring software is available from the authors upon request.

Author contributions LM performed drone-based measurements, analyzed the data and drafted the manuscript. FF and FD performed ground-based measurements and related data post-processing. HT provided synoptic maps and mixing layer height calculations. All authors discussed the data and the presented results. All co-authors commented on the manuscript.

Competing interests The authors declare that they have no conflict of interest.

Financial support This work was supported by internal funding from the Max Planck Society. LM is funded by the Deutsche Forschungsgemeinschaft (DFG, German Research Foundation) – TRR 301 "TPChange" (Project-ID 428312742); similarly, HT acknowledges funding from the same project ID (subproject Z03).

Appendix A: Instruments and data sources used for characterization of the lower troposphere

Table A1: Instruments used for characterization of the lower troposphere.

Instrument	Measured variables	Time resolution
MoLa (Drewnick et al., 2012)		
AMS[a]	Chemical composition of non-refractory particles < 1 µm	30 s
Ceilometer[b]	Altitude-dependent backscatter signal intensity	30 s
CPC[c]	Particle number concentration	1 s
EDM[d]	Particulate matter PM_1	6 s
FMPS[e]	Particle size distribution based on electrical mobility diameter	1 s
Meteorological station[f]	Wind direction, wind speed, relative humidity, temperature, rain intensity, pressure	1 s
OPC[g]	Particle size distribution based on optical diameter	6 s
O_3-monitor[h]	Mixing ratio of O_3	2 s
Pyranometer[i]	Solar irradiance	1s
[a] HR-ToF-AMS, Aerosol Mass Spectrometer, Aerodyne Res., Inc., Billerica, Massachusetts, USA. [b] CHM 15k, Lufft Mess- und Regeltechnik GmbH, Fellbach, Germany. [c] Condensation Particle Counter Model 3786, TSI, Inc., Shoreview, Minnesota, USA. [d] Environmental Dust Monitor EDM180, Grimm Aerosol Technik GmbH, Ainring, Germany. [e] Fast Mobility Particle Sizer Model 3091, TSI, Inc., Shoreview, Minnesota, USA. [f] WXT520, Vaisala Oyj, Vantaa, Finland. [g] Optical Particle Counter Model 1.109, Grimm Aerosol Technik GmbH, Ainring, Germany. [h] Monitor 205 Dual Beam Ozone Monitor, 2B Technologies, Inc., Boulder, Colorado, USA. [i] CMP3 Pyranometer Sensor, Campbell Scientific, Inc., Logan, Utah, UK.		
Flux tower		
Ultra-sonic anemometer[j]	3D wind direction, humidity, temperature	0.05 s
[j] CSAT3B 3-D Sonic Anemometer, Campbell Scientific, Inc., Logan, Utah, USA.		
FLab (Moormann et al., 2025)		
Anemometer[k]	Horizontal wind speed and direction; temperature; relative humidity; pressure	1 s
CPC[l]	Particle number concentration	1 s
OPC[m]	Particle size distribution based on optical diameter; temperature; relative humidity	1 s
O_3-monitor[n]	Mixing ratio of O_3	2 s
drone: Matrice 600[o]	3D orientation; 3D flight velocity; GPS position; wind speed and direction; altitude based on pressure level and GPS; propeller rotation rate; various internal data	≤1 s
[k] TriSonica™ Mini, Anemoment LLC, Lincoln, Nebraska, USA. [l] Condensation Particle Counter Model 3007, TSI, Inc., Shoreview, Minnesota, USA. [m] OPC-N3, Alphasense AMETEK®, Great Notley, United Kingdom. [n] Model 205 Dual Beam Ozone Monitor, 2B Technologies, Inc., Boulder, Colorado, USA. [o] Matrice 600, SZ DJI Technology Co., Ltd., Shenzhen, China.		
Radiosonde		
Radiosonde[p]	Wind speed and direction; temperature; relative humidity; pressure	1 s
[p] Radiosonde RS41-SGP, Vaisala Oyj, Vantaa, Finland.		

Table A2: Synoptic scale data and resolution.

Data source	Derived variables	Temporal resolution	Spatial resolution
HySplit **(Stein et al., 2015)**	24 h-backward trajectories in 0 m, 120 m, 500 m	1 h	0.25°
ICON-D2 **(Zängl et al., 2015; DWD, 2025b)**	Mixing layer heights and backward trajectories in German domain, forecast data with 16 layers in lowermost kilometer with varying layer thickness > 30 m and < 100 m.	3 h	2 km
PAMORE **(DWD, 2025a)**	Forecast data with shorter lead time to increase temporal resolution of ICON-D2 data	2 h	
ERA5 **(Hersbach et al., 2020)**	Reanalysis data (geopotential in 500 hPa, surface pressure)	3 h	31 km
WN data set **(Kreklow et al., 2019)**	Radar data	1 min	1 km
EUMETSAT **(Schmetz et al., 2002)**	Satellite images	15 min	1.67 km – 4.8 km

Formatiert: Links

Formatierte Tabelle

hat formatiert: Schriftart: 10 Pt., Nicht Fett

Feldfunktion geändert

hat formatiert: Deutsch (Deutschland)

hat formatiert: Deutsch (Deutschland), Nicht Hochgestellt/ Tiefgestellt

hat formatiert: Nicht Hochgestellt/ Tiefgestellt

hat formatiert: Deutsch (Deutschland)

Formatierte Tabelle

Feldfunktion geändert

hat formatiert: Schriftart: 10 Pt., Nicht Fett

hat formatiert: Nicht Hochgestellt/ Tiefgestellt

Feldfunktion geändert

hat formatiert: Schriftart: 10 Pt., Nicht Fett

Feldfunktion geändert

hat formatiert: Schriftart: 10 Pt., Nicht Fett

References

Andreae, M. O., Acevedo, O. C., Araùjo, A., Artaxo, P., Barbosa, C. G. G., Barbosa, H. M. J., Brito, J., Carbone, S., Chi, X., Cintra, B. B. L., da Silva, N. F., Dias, N. L., Dias-Júnior, C. Q., Ditas, F., Ditz, R., Godoi, A. F. L., Godoi, R. H. M., Heimann, M., Hoffmann, T., Kesselmeier, J., Könemann, T., Krüger, M. L., Lavric, J. V., Manzi, A. O., Lopes, A. P., Martins, D. L., Mikhailov, E. F., Moran-Zuloaga, D., Nelson, B. W., Nölscher, A. C., Santos Nogueira, D., Piedade, M. T. F., Pöhlker, C., Pöschl, U., Quesada, C. A., Rizzo, L. V., Ro, C. U., Ruckteschler, N., Sá, L. D. A., de Oliveira Sá, M., Sales, C. B., dos Santos, R. M. N., Saturno, J., Schöngart, J., Sörgel, M., de Souza, C. M., de Souza, R. A. F., Su, H., Targhetta, N., Tóta, J., Trebs, I., Trumbore, S., van Eijck, A., Walter, D., Wang, Z., Weber, B., Williams, J., Winderlich, J., Wittmann, F., Wolff, S., and Yáñez-Serrano, A. M.: The Amazon Tall Tower Observatory (ATTO): overview of pilot measurements on ecosystem ecology, meteorology, trace gases, and aerosols, Atmos. Chem. Phys., 15, 10723-10776, https://doi.org/10.5194/acp-15-10723-2015, 2015.

Barnes, G. M. and Garstang, M.: Subcloud Layer Energetics of Precipitating Convection, Monthly Weather Review, 110, 102-117, https://doi.org/10.1175/1520-0493(1982)110<0102:SLEOPC>2.0.CO;2, 1982.

Barros, A. P. and Lettenmaier, D. P.: Dynamic modeling of orographically induced precipitation, Reviews of Geophysics, 32, 265-284, https://doi.org/10.1029/94rg00625, 1994.

Bela, M. M., Barth, M. C., Toon, O. B., Fried, A., Ziegler, C., Cummings, K. A., Li, Y., Pickering, K. E., Homeyer, C. R., Morrison, H., Yang, Q., Mecikalski, R. M., Carey, L., Biggerstaff, M. I., Betten, D. P., and Alford, A. A.: Effects of Scavenging, Entrainment, and Aqueous Chemistry on Peroxides and Formaldehyde in Deep Convective Outflow Over the

Central and Southeast United States, Journal of Geophysical Research: Atmospheres, 123, 7594-7614, https://doi.org/10.1029/2018jd028271, 2018.

Bélair, F., Dyer-Hawes, Q., and Romanic, D.: The Dynamics of the Urban Boundary Layer Before and During a Severe Thunderstorm Outflow Over Downtown Montréal, Boundary-Layer Meteorology, 191, https://doi.org/10.1007/s10546-024-00896-4, 2025.

Bonne, J.-L., Donnat, L., Albora, G., Burgalat, J., Chauvin, N., Combaz, D., Cousin, J., Decarpenterie, T., Duclaux, O., Dumelié, N., Galas, N., Juery, C., Parent, F., Pineau, F., Maunoury, A., Ventre, O., Bénassy, M.-F., and Joly, L.: A measurement system for CO2 and CH4 emissions quantification of industrial sites using a new in situ concentration sensor operated on board uncrewed aircraft vehicles, Atmospheric Measurement Techniques, 17, 4471-4491, https://doi.org/10.5194/amt-17-4471-2024, 2024.

Bopape, M.-J. M., Waitolo, D., Plant, R. S., Phaduli, E., Nkonde, E., Simfukwe, H., Mkandawire, S., Rakate, E., and Maisha, R.: Sensitivity of Simulations of Zambian Heavy Rainfall Events to the Atmospheric Boundary Layer Schemes, Climate, 9, 38, https://doi.org/10.3390/cli9020038, 2021.

Borque, P., Nesbitt, S. W., Trapp, R. J., Lasher-Trapp, S., and Oue, M.: Observational Study of the Thermodynamics and Morphological Characteristics of a Midlatitude Continental Cold Pool Event, Monthly Weather Review, 148, 719-737, https://doi.org/10.1175/MWR-D-19-0068.1, 2020.

Chen, Z. H., Cheng, S. Y., Li, J. B., Guo, X. R., Wang, W. H., and Chen, D. S.: Relationship between atmospheric pollution processes and synoptic pressure patterns in northern China, Atmospheric Environment, 42, 6078-6087, https://doi.org/10.1016/j.atmosenv.2008.03.043, 2008.

Cherrier, G., Belut, E., Gerardin, F., Tanière, A., and Rimbert, N.: Aerosol particles scavenging by a droplet: Microphysical modeling in the Greenfield gap, Atmospheric Environment, 166, 519-530, https://doi.org/10.1016/j.atmosenv.2017.07.052, 2017.

Crook, N. A. and Klemp, J. B.: Lifting by Convergence Lines, Journal of the Atmospheric Sciences, 57, 873-890, https://doi.org/10.1175/1520-0469(2000)057<0873:LBCL>2.0.CO;2, 2000.

Crueger, T., Giorgetta, M. A., Brokopf, R., Esch, M., Fiedler, S., Hohenegger, C., Kornblueh, L., Mauritsen, T., Nam, C., Naumann, A. K., Peters, K., Rast, S., Roeckner, E., Sakradzija, M., Schmidt, H., Vial, J., Vogel, R., and Stevens, B.: ICON-A, The Atmosphere Component of the ICON Earth System Model: II. Model Evaluation, Journal of Advances in Modeling Earth Systems, 10, 1638-1662, https://doi.org/10.1029/2017ms001233, 2018.

Drewnick, F., Böttger, T., von der Weiden-Reinmüller, S. L., Zorn, S. R., Klimach, T., Schneider, J., and Borrmann, S.: Design of a mobile aerosol research laboratory and data processing tools for effective stationary and mobile field measurements, Atmospheric Measurement Techniques, 5, 1443-1457, https://doi.org/10.5194/amt-5-1443-2012, 2012.

DWD: Pamore - Retrieving archived forecast model data, German Meteorological Service, https://www.dwd.de/EN/ourservices/pamore/pamore.html, Access Date, 2025a

DWD: Model documentation ICON-D2 (Regional model Germany), German Meteorological Service, https://www.dwd.de/DE/leistungen/nwv_icon_d2_modelldokumentation/nwv_icon_d2_modelldokumentation.html, 2025b

DWD: Open Data Server of the German Meteorological Service, German Meteorological Service, https://opendata.dwd.de, Access Date, 2025c

Elston, J., Argrow, B., Stachura, M., Weibel, D., Lawrence, D., and Pope, D.: Overview of Small Fixed-Wing Unmanned Aircraft for Meteorological Sampling, Journal of Atmospheric and Oceanic Technology, 32, 97-115, https://doi.org/10.1175/jtech-d-13-00236.1, 2015.

Engerer, N. A., Stensrud, D. J., and Coniglio, M. C.: Surface Characteristics of Observed Cold Pools, Monthly Weather Review, 136, 4839-4849, https://doi.org/10.1175/2008MWR2528.1, 2008.

Fitzky, A. C., Sandén, H., Karl, T., Fares, S., Calfapietra, C., Grote, R., Saunier, A., and Rewald, B.: The Interplay Between Ozone and Urban Vegetation—BVOC Emissions, Ozone Deposition, and Tree Ecophysiology, Frontiers in Forests and Global Change, 2, https://doi.org/10.3389/ffgc.2019.00050, 2019.

Golzio, A., Ferrarese, S., Cassardo, C., Diolaiuti, G. A., and Pelfini, M.: Land-Use Improvements in the Weather Research and Forecasting Model over Complex Mountainous Terrain and Comparison of Different Grid Sizes, Boundary-Layer Meteorology, 180, 319-351, https://doi.org/10.1007/s10546-021-00617-1, 2021.

Haerter, J. O. and Schlemmer, L.: Intensified Cold Pool Dynamics Under Stronger Surface Heating, Geophysical Research Letters, 45, 6299-6310, https://doi.org/10.1029/2017gl076874, 2018.

Helbig, M., Gerken, T., Beamesderfer, E. R., Baldocchi, D. D., Banerjee, T., Biraud, S. C., Brown, W. O. J., Brunsell, N. A., Burakowski, E. A., Burns, S. P., Butterworth, B. J., Chan, W. S., Davis, K. J., Desai, A. R., Fuentes, J. D., Hollinger, D. Y., Kljun, N., Mauder, M., Novick, K. A., Perkins, J. M., Rahn, D. A., Rey-Sanchez, C., Santanello, J. A., Scott, R. L., Seyednasrollah, B., Stoy, P. C., Sullivan, R. C., de Arellano, J. V.-G., Wharton, S., Yi, C., and Richardson, A. D.: Integrating continuous atmospheric boundary layer and tower-based flux measurements to advance understanding of land-atmosphere interactions, Agricultural and Forest Meteorology, 307, 108509, https://doi.org/10.1016/j.agrformet.2021.108509, 2021.

Hersbach, H., Bell, B., Berrisford, P., Hirahara, S., Horányi, A., Muñoz-Sabater, J., Nicolas, J., Peubey, C., Radu, R., Schepers, D., Simmons, A., Soci, C., Abdalla, S., Abellan, X., Balsamo, G., Bechtold, P., Biavati, G., Bidlot, J., Bonavita, M., De Chiara, G., Dahlgren, P., Dee, D., Diamantakis, M., Dragani, R., Flemming, J., Forbes, R., Fuentes, M., Geer, A., Haimberger, L., Healy, S., Hogan, R. J., Hólm, E., Janisková, M., Keeley, S., Laloyaux, P., Lopez, P., Lupu, C., Radnoti, G., De Rosnay, P., Rozum, I., Vamborg, F., Villaume, S., and Thépaut, J. N.: The ERA5 global reanalysis, Quarterly Journal of the Royal Meteorological Society, 146, 1999-2049, https://doi.org/10.1002/qj.3803, 2020.

Hoyle, C. R., Fuchs, C., Järvinen, E., Saathoff, H., Dias, A., El Haddad, I., Gysel, M., Coburn, S. C., Tröstl, J., Bernhammer, A. K., Bianchi, F., Breitenlechner, M., Corbin, J. C., Craven, J., Donahue, N. M., Duplissy, J., Ehrhart, S., Frege, C., Gordon, H., Höppel, N., Heinritzi, M., Kristensen, T. B., Molteni, U., Nichman, L., Pinterich, T., Prévôt, A. S. H., Simon, M., Slowik, J. G., Steiner, G., Tomé, A., Vogel, A. L., Volkamer, R., Wagner, A. C., Wagner, R., Wexler, A. S., Williamson, C., Winkler, P. M., Yan, C., Amorim, A., Dommen, J., Curtius, J., Gallagher, M. W., Flagan, R. C., Hansel, A., Kirkby, J., Kulmala, M., Möhler, O., Stratmann, F., Worsnop, D. R., and Baltensperger, U.: Aqueous phase oxidation of sulphur dioxide by ozone in cloud droplets, Atmos. Chem. Phys., 16, 1693-1712, https://doi.org/10.5194/acp-16-1693-2016, 2016.

Hyun, Y.-K., Kim, K.-E., and Ha, K.-J.: A comparison of methods to estimate the height of stable boundary layer over a temperate grassland, Agricultural and Forest Meteorology, 132, 132-142, https://doi.org/10.1016/j.agrformet.2005.03.010, 2005.

Klemp, J. B.: A terrain-following coordinate with smoothed coordinate surfaces, Monthly weather review, 139, 2163-2169, https://doi.org/10.1175/MWR-D-10-05046.1, 2011.

Knote, C., Hodzic, A., and Jimenez, J. L.: The effect of dry and wet deposition of condensable vapors on secondary organic aerosols concentrations over the continental US, Atmospheric Chemistry and Physics, 15, 1-18, https://doi.org/10.5194/acp-15-1-2015, 2015.

Kotthaus, S., Bravo-Aranda, J. A., Collaud Coen, M., Guerrero-Rascado, J. L., Costa, M. J., Cimini, D., O'Connor, E. J., Hervo, M., Alados-Arboledas, L., Jiménez-Portaz, M., Mona, L., Ruffieux, D., Illingworth, A., and Haeffelin, M.: Atmospheric boundary layer height from ground-based remote sensing: a review of capabilities and limitations, Atmospheric Measurement Techniques, 16, 433-479, https://doi.org/10.5194/amt-16-433-2023, 2023.

Kreklow, J., Tetzlaff, B., Kuhnt, G., and Burkhard, B.: A Rainfall Data Intercomparison Dataset of RADKLIM, RADOLAN, and Rain Gauge Data for Germany, Data, 4, 118, https://doi.org/10.3390/data4030118, 2019.

Lambe, A. T., Onasch, T. B., Massoli, P., Croasdale, D. R., Wright, J. P., Ahern, A. T., Williams, L. R., Worsnop, D. R., Brune, W. H., and Davidovits, P.: Laboratory studies of the chemical composition and cloud condensation nuclei (CCN) activity of secondary organic aerosol (SOA) and oxidized primary organic aerosol (OPOA), Atmos. Chem. Phys., 11, 8913-8928, https://doi.org/10.5194/acp-11-8913-2011, 2011.

Liu, J. and Kirshbaum, D. J.: Environmental Conditions Controlling the Morphology of Shallow Orographic Convection, Journal of the Atmospheric Sciences, 82, 483-500, https://doi.org/10.1175/jas-d-24-0113.1, 2025.

Lochbihler, K., Lenderink, G., and Siebesma, A. P.: Cold Pool Dynamics Shape the Response of Extreme Rainfall Events to Climate Change, Journal of Advances in Modeling Earth Systems, 13, https://doi.org/10.1029/2020ms002306, 2021.

Luiz, E. W. and Fiedler, S.: Global Climatology of Low-Level-Jets: Occurrence, Characteristics, and Meteorological Drivers, Journal of Geophysical Research: Atmospheres, 129, https://doi.org/10.1029/2023jd040262, 2024.

Machado, L. A. T., Unfer, G. R., Brill, S., Hildmann, S., Pöhlker, C., Cheng, Y., Williams, J., Hartwig, H., Andreae, M. O., Artaxo, P., Curtius, J., Franco, M. A., Cecchini, M. A., Edtbauer, A., Hoffmann, T., Holanda, B., Khadir, T., Krejci, R., Kremper, L. A., Liu, Y., Meller, B. B., Pöhlker, M. L., Quesada, C. A., Ringsdorf, A., Riipinen, I., Trumbore, S., Wolff, S., Lelieveld, J., and Pöschl, U.: Frequent rainfall-induced new particle formation within the canopy in the Amazon rainforest, Nature Geoscience, https://doi.org/10.1038/s41561-024-01585-0, 2024a.

Machado, L. A. T., Kesselmeier, J., Botía, S., Van Asperen, H., O. Andreae, M., De Araújo, A. C., Artaxo, P., Edtbauer, A., R. Ferreira, R., Franco, M. A., Harder, H., Jones, S. P., Dias-Júnior, C. Q., Haytzmann, G. G., Quesada, C. A., Komiya, S., Lavric, J., Lelieveld, J., Levin, I., Nölscher, A., Pfannerstill, E., Pöhlker, M. L., Pöschl, U., Ringsdorf, A., Rizzo, L., Yáñez-Serrano, A. M., Trumbore, S., Valenti, W. I. D., Vila-Guerau De Arellano, J., Walter, D., Williams, J., Wolff, S., and Pöhlker, C.: How rainfall events modify trace gas mixing ratios in central Amazonia, Atmospheric Chemistry and Physics, 24, 8893-8910, https://doi.org/10.5194/acp-24-8893-2024, 2024b.

Markowski, P. M., Lis, N. T., Turner, D. D., Lee, T. R., and Buban, M. S.: Observations of Near-Surface Vertical Wind Profiles and Vertical Momentum Fluxes from VORTEX-SE 2017: Comparisons to Monin–Obukhov Similarity Theory, Monthly Weather Review, 147, 3811-3824, https://doi.org/10.1175/mwr-d-19-0091.1, 2019.

McWilliams, J. C., Meneveau, C., Patton, E. G., and Sullivan, P. P.: Stable Boundary Layers and Subfilter-Scale Motions, Atmosphere, 14, 1107, https://doi.org/10.3390/atmos14071107, 2023.

Miyama, T., Morishita, T., Kominami, Y., Noguchi, H., Yasuda, Y., Yoshifuji, N., Okano, M., Yamanoi, K., Mizoguchi, Y., Takanashi, S., Kitamura, K., and Matsumoto, K.: Increases in Biogenic Volatile Organic Compound Concentrations Observed after Rains at Six Forest Sites in Non-Summer Periods, Atmosphere, 11, 1381, https://doi.org/10.3390/atmos11121381, 2020.

Monin, A. S. and Obukhov, A. M.: Basic laws of turbulent mixing in the surface layer of the atmosphere, Tr. Akad. Nauk. SSSR Geophiz. Inst., 24, 163-187, https://gibbs.science/efd/handouts/monin_obukhov_1954.pdf, 1954.

Moormann, L., Böttger, T., Schuhmann, P., Valero, L., Fachinger, F., and Drewnick, F.: The Flying Laboratory FLab: development and application of a UAS to measure aerosol particles and trace gases in the lower troposphere, Atmos. Meas. Tech., 18, 1441-1459, https://doi.org/10.5194/amt-18-1441-2025, 2025.

Neuman, J. A., Trainer, M., Aikin, K. C., Angevine, W. M., Brioude, J., Brown, S. S., de Gouw, J. A., Dube, W. P., Flynn, J. H., Graus, M., Holloway, J. S., Lefer, B. L., Nedelec, P., Nowak, J. B., Parrish, D. D., Pollack, I. B., Roberts, J. M., Ryerson, T. B., Smit, H., Thouret, V., and Wagner, N. L.: Observations of ozone transport from the free troposphere to the Los Angeles basin, Journal of Geophysical Research: Atmospheres, 117, https://doi.org/10.1029/2011JD016919, 2012.

Platis, A., Altstädter, B., Wehner, B., Wildmann, N., Lampert, A., Hermann, M., Birmili, W., and Bange, J.: An Observational Case Study on the Influence of Atmospheric Boundary-Layer Dynamics on New Particle Formation, Boundary-Layer Meteorology, 158, 67-92, https://doi.org/10.1007/s10546-015-0084-y, 2016.

Pohorsky, R., Baccarini, A., Brett, N., Barret, B., Bekki, S., Pappaccogli, G., Dieudonné, E., Temime-Roussel, B., D'Anna, B., Cesler-Maloney, M., Donateo, A., Decesari, S., Law, K. S., Simpson, W. R., Fochesatto, J., Arnold, S. R., and Schmale, J.: In situ vertical observations of the layered structure of air pollution in a continental high-latitude urban boundary layer during winter, Atmos. Chem. Phys., 25, 3687-3715, https://doi.org/10.5194/acp-25-3687-2025, 2025.

Qian, Y., Yan, H., Berg, L. K., Hagos, S., Feng, Z., Yang, B., and Huang, M.: Assessing Impacts of PBL and Surface Layer Schemes in Simulating the Surface–Atmosphere Interactions and Precipitation over the Tropical Ocean Using Observations from AMIE/DYNAMO, Journal of Climate, 29, 8191-8210, https://doi.org/10.1175/jcli-d-16-0040.1, 2016.

Radtke, J. K., Kies, B. N., Mottishaw, W. A., Zeuli, S. M., Voon, A. T. H., Koerber, K. L., Petty, G. W., Vermeuel, M. P., Bertram, T. H., Desai, A. R., Hupy, J. P., Pierce, R. B., Wagner, T. J., and Cleary, P. A.: Observing low-altitude features in ozone concentrations in a shoreline environment via uncrewed aerial systems, Atmos. Meas. Tech., 17, 2833-2847, https://doi.org/10.5194/amt-17-2833-2024, 2024.

Raschendorfer, M.: The new turbulence parameterization of LM, http://www.cosmo-model.org, 2001.

Rossabi, S., Choudoir, M., Helmig, D., Hueber, J., and Fierer, N.: Volatile Organic Compound Emissions From Soil Following Wetting Events, Journal of Geophysical Research: Biogeosciences, 123, 1988-2001, https://doi.org/10.1029/2018jg004514, 2018.

Ryan, B. F., Katzfey, J. J., Abbs, D. J., Jakob, C., Lohmann, U., Rockel, B., Rotstayn, L. D., Stewart, R. E., Szeto, K. K., Tselioudis, G., and Yau, M. K.: Simulations of a Cold Front by Cloud-Resolving, Limited-Area, and Large-Scale Models, and a Model Evaluation Using In Situ and Satellite Observations, Monthly Weather Review, 128, 3218-3235, https://doi.org/10.1175/1520-0493(2000)128<3218:SOACFB>2.0.CO;2, 2000.

Schlemmer, L. and Hohenegger, C.: The Formation of Wider and Deeper Clouds as a Result of Cold-Pool Dynamics, Journal of the Atmospheric Sciences, 71, 2842-2858, https://doi.org/10.1175/jas-d-13-0170.1, 2014.

Schmetz, J., Pili, P., Tjemkes, S., Just, D., Kerkmann, J., Rota, S., and Ratier, A.: An introduction to Meteosat second generation (MSG), Bulletin of the American Meteorological Society, 83, 977-992, https://doi.org/10.1175/1520-0477(2002)083<0977:AITMSG>2.3.CO;2, 2002.

Seidel, D. J., Ao, C. O., and Li, K.: Estimating climatological planetary boundary layer heights from radiosonde observations: Comparison of methods and uncertainty analysis, Journal of Geophysical Research: Atmospheres, 115, https://doi.org/10.1029/2009JD013680, 2010.

Steeneveld, G.-J.: Current challenges in understanding and forecasting stable boundary layers over land and ice, Frontiers in Environmental Science, 2, https://doi.org/10.3389/fenvs.2014.00041, 2014.

Stein, A. F., Draxler, R. R., Rolph, G. D., Stunder, B. J. B., Cohen, M. D., and Ngan, F.: NOAA's HYSPLIT Atmospheric Transport and Dispersion Modeling System, Bulletin of the American Meteorological Society, 96, 2059-2077, https://doi.org/10.1175/bams-d-14-00110.1, 2015.

Stull, R. B.: An Introduction to Boundary Layer Meteorology, Atmospheric and Oceanographic Sciences Library, https://doi.org/10.1007/978-94-009-3027-8, 1988.

Szintai, B., Kaufmann, P., and Rotach, M. W.: Simulation of Pollutant Transport in Complex Terrain with a Numerical Weather Prediction–Particle Dispersion Model Combination, Boundary-Layer Meteorology, 137, 373-396, https://doi.org/10.1007/s10546-010-9541-9, 2010.

Sziroczak, D., Rohacs, D., and Rohacs, J.: Review of using small UAV based meteorological measurements for road weather management, Progress in Aerospace Sciences, 134, 100859, https://doi.org/10.1016/j.paerosci.2022.100859, 2022.

Tignat-Perrier, R., Dommergue, A., Vogel, T. M., and Larose, C.: Microbial Ecology of the Planetary Boundary Layer, Atmosphere, 11, 1296, https://doi.org/10.3390/atmos11121296, 2020.

Tompkins, A. M.: Organization of Tropical Convection in Low Vertical Wind Shears: The Role of Cold Pools, Journal of the Atmospheric Sciences, 58, 1650-1672, https://doi.org/10.1175/1520-0469(2001)058<1650:OOTCIL>2.0.CO;2, 2001.

Tsamalis, C., Ravetta, F., Gheusi, F., Delbarre, H., and Augustin, P.: Mixing of free-tropospheric air with the lowland boundary layer during anabatic transport to a high altitude station, Atmospheric Research, 143, 425-437, https://doi.org/10.1016/j.atmosres.2014.03.011, 2014.

Valero, L., Kandler, K., Jost, S., Tost, H., Eichhorn, L. K., von Glahn, C., Rott, H., Flory, M., Baron, A., Smith, K., Thornberry, T., and Weigel, R.: Light-weight Observatory for sOuNdIng clouds and aeorSol, LOONIS: a balloon lifted platform for troposphere aerosol research, EGUsphere, 2025, 1-36, https://doi.org/10.5194/egusphere-2025-5568, 2025.

Villa, T. F., Gonzalez, F., Miljievic, B., Ristovski, Z. D., and Morawska, L.: An Overview of Small Unmanned Aerial Vehicles for Air Quality Measurements: Present Applications and Future Prospectives, Sensors (Basel), 16, https://doi.org/10.3390/s16071072, 2016.

Wang, R., Zhu, Y., Qiao, F., Liang, X.-Z., Zhang, H., and Ding, Y.: High-resolution Simulation of an Extreme Heavy Rainfall Event in Shanghai Using the Weather Research and Forecasting Model: Sensitivity to Planetary Boundary Layer Parameterization, Advances in Atmospheric Sciences, 38, 98-115, https://doi.org/10.1007/s00376-020-9255-y, 2021.

Wang, X. Y. and Wang, K. C.: Estimation of atmospheric mixing layer height from radiosonde data, Atmospheric Measurement Techniques, 7, 1701-1709, https://doi.org/10.5194/amt-7-1701-2014, 2014.

Wei, P., Cheng, S., Li, J., and Su, F.: Impact of boundary-layer anticyclonic weather system on regional air quality, Atmospheric Environment, 45, 2453-2463, https://doi.org/10.1016/j.atmosenv.2011.01.045, 2011.

Young, G. S., Perugini, S. M., and Fairall, C. W.: Convective Wakes in the Equatorial Western Pacific during TOGA, Monthly Weather Review, 123, 110-123, https://doi.org/10.1175/1520-0493(1995)123<0110:CWITEW>2.0.CO;2, 1995.

Zängl, G., Reinert, D., Rípodas, P., and Baldauf, M.: The ICON (ICOsahedral Non-hydrostatic) modelling framework of DWD and MPI-M: Description of the non-hydrostatic dynamical core, Quarterly Journal of the Royal Meteorological Society, 141, 563-579, https://doi.org/10.1002/qj.2378, 2015.

Zum Berge, K., Gaiser, A., Knaus, H., Platis, A., and Bange, J.: Seasonal Changes in Boundary-Layer Flow Over a Forested Escarpment Measured by an Uncrewed Aircraft System, Boundary-Layer Meteorology, 186, 69-91, https://doi.org/10.1007/s10546-022-00743-4, 2023.